Thorium isotopes in the Southeast Atlantic Ocean: Tracking scavenging during water mass mixing along neutral density surfaces

Roy-Barman Matthieu [1, *], Thil François [1], Bordier Louise [1], Dapoigny Arnaud [1], Foliot Lorna [1], Ayrault Sophie [1], Lacan François [2], Jeandel Catherine [2], Pradoux Catherine [2], Garcia-Solsona Ester [2, 3]

[1] Laboratoire des Sciences du Climat et de l'Environnement, LSCE-IPSL (CEA CNRS UVSQ), Université Paris-Saclay, Orme des Merisiers - centre de Saclay, 91191, Gif-sur-Yvette, France
[2] LEGOS (CNRS/CNES/IRD/Université de Toulouse), Observatoire Midi-Pyrénées, 31400, Toulouse, France
[3] Dinàmica de la Terra i de l'Oceà, Facultat de Ciències de la Terra, Universitat de Barcelona, 08028, Barcelona, Spain

* Corresponding author : Matthieu Roy-Barman, email address : matthieu.roy-barman@lsce.ipsl.fr

Abstract :

The distributions of dissolved and particulate thorium isotopes (230Th and 232Th) were established in samples from the BONUS GoodHope (BGH) IPY-GEOTRACES cruise in the SE Atlantic sector of the Southern Ocean (36°S-13°E to 57°S-0°, Feb.–Mar. 2008). The distribution of total (dissolved + particulate) 232Th is dominated by the inputs from continental margins. The non-linear profiles of dissolved 230Th are interpreted as due to the southward upwelling of the isopycnal surfaces. However, total 230Th and 232Th versus salinity plots illustrate departures from binary mixing and provides evidence for non-conservative behavior of both isotopes along the section. We propose a model for total 230Th and 232Th scavenging and mixing along isopycnal surfaces. We use this model to estimate particle settling speeds and isopycnal eddy diffusion coefficients along the BGH section. Data-model comparison suggests particle settling velocities in the range of 400–700 m/y and isopycnal eddy diffusivity of the order of 2000 m2/s.

Highlights

► Small deviations of thorium isotopes from a conservative behavior occurs during isopycnal mixing through the ACC. ► An advection-diffusion-scavenging model along neutral density surface is applied to thorium isotopes. ► Combining thorium isotopes allows constraining particle settling speeds and isopycnal mixing coefficients.

Keywords : Thorium isotopes, Southern ocean, Atlantic, Marine particles, Isopycnal mixing

1. Introduction

Thorium isotopes are recognized tracers of particle dynamics in the ocean that provide key information on ocean biogeochemical cycles (Bacon and Anderson, 1982, Nozaki et al., 1981, Roy-Barman et al., 1996). In particular, ^{230}Th is produced *in situ* by radioactive decay of ^{234}U and rapidly scavenged on marine particles, thus providing a chronometer for estimating the settling speed for marine particles. ^{232}Th is introduced in the ocean by continental inputs and hence can bring complementary information on marine particles compared to ^{230}Th (Roy-Barman et al., 2002).

In early studies, particle settling speeds were derived from ^{230}Th with a simple 1D (vertical) production-scavenging model, which was well adapted to oceanic areas with weak currents (Bacon and Anderson, 1982, Nozaki et al., 1981, Roy-Barman et al., 1996, Roy-Barman, 2009). However, it is now clear that strong currents characterizing oceanic regions such as the Southern Ocean may significantly affect the distribution of ^{230}Th in the water column and hence potentially bias the estimate of the settling speed of marine particles obtained by the simple production-scavenging model. Therefore, a simple production-scavenging-advection model was proposed to constrain simultaneously the renewal rate of the deep waters and the settling speed of marine particles in the Atlantic sector of the Southern Ocean (Rutgers van der Loeff et al., 1996). However, it relies on rather crude approximations, such as uniform values for ventilation rate and particle settling speed over the whole water column. Another limitation of this model is that it does not consider the mixing of water masses with different origins and Th contents.

In the real ocean, the distribution of geochemical tracers depends on both non-conservative processes and mixing of water masses of different origins, in addition to advection by currents. This mixing is thought to occur preferentially along surfaces of constant density called isopycnal surfaces. Chase et al. (2003) suggested that the small gradients in ^{230}Th concentration observed along neutral density surfaces in the deep waters of the Southern Ocean argue for small eddy diffusive fluxes and little scavenging of ^{230}Th across the Antarctic Polar Front (APF). However, they also advocated for further work to better constrain both nuclide concentrations along isopycnal surfaces and diffusion coefficients in the Southern Ocean.

In the present work, we take advantage of high precision ^{230}Th data collected during the Bonus GoodHope cruise to revisit the behavior of ^{230}Th across the Southern Ocean and to try to unravel the respective roles of water mass mixing and particle scavenging along neutral

99   density surfaces. Our goal is to explore if Th data can help constraining both particle settling

100 speeds and water mixing rates using a model that is more complete than with the simple

101 mixing-scavenging model.

102

103

104 2. Sampling and methods

105   2.1. Hydrographic settings

106   The oceanographic structure determined from the Bonus GoodHope (BGH) expedition

107 has already been described (Chever et al., 2010, Bown et al., 2011, Garcia-Solsona et al.,

108 2014, Abadie et al., 2017), so we only summarize the main features and focus on the 5 super

109 stations (S1–S5 stations, Fig. 1) sampled for Th isotopes. Three main hydrological and

110 circulation regimes characterize the studied area: the Subtropical domain (Station S1), the

111 Antarctic Circumpolar Current (ACC; S2 to S4) and the Weddell Sea Gyre (S5). The

112 subtropical domain is bounded to the south by the subtropical front (STF), which was located

113 around 41°S-42°S, north of S2. The ACC domain, incorporating the Subantarctic Front (SAF;

114 ~45°S) and the Polar Front (PF; ~50°S), is bounded to the south by the southern ACC

115 boundary (Sby). From the Sby to the Antarctic continent, water circulation is dominated by

116 the cyclonic Weddell Gyre (WG; S5).

117

118

119

120

121   The subtropical regime is influenced from 0 down to ~800 m by surface and

122 intermediate waters of Indian Ocean origin ($\theta \geq 10$ °C, $S \geq 34.5$), conveyed south of Africa by

123 the Agulhas Current and detached eddies (Gladyshev et al., 2008). At intermediate depths

124 (~300–900 m), Antarctic Intermediate Water (AAIW) originates from cooled surface waters

125 of the ACC that are subsequently subducted northward at the PF. Two varieties of AAIW

126 have been recognized from BGH cruise data: one originating from the Indian Ocean (i-

127 AAIW) close to the African continent (S > 34.3; S1) and one formed in the Atlantic Ocean (a-

128 AAIW; S < 34.3; S2–S4). The Upper Circumpolar Deep Water (UCDW; ranging from 500 to

129 2000 m depth) is identified below the AAIW and upwells southwards. Below UCDW, the

130 eastward flowing (and southward drifting) NADW is detected by its salinity maximum within

131 the 2000–3000 m depth range. Two NADW branches are identified in the BONUS section:

132 North of the Agulhas Ridge, higher salinities indicate advection by an eastern boundary

4

current referred to as SE-NADW (S1 and S2 stations). South of the Agulhas Ridge, the main (western) component of NADW (i.e., SW- NADW; S2-S4 stations) is incorporated into the ACC after flowing southward along the Argentine-Brazilian margin (Stramma and England, 1999). The other water mass encountered at southern ACC latitudes is high salinity Lower Circumpolar Deep Water (LCDW). Cold and fresher Antarctic Bottom Water (AABW) is also recognized, occupying the water column from LCDW/NADW depths down to the sea floor (Fig. 2). In the Weddell Sea Gyre domain (S5), we interpret deep oxygenated waters as due to input of recently ventilated AABW.

Water mass transport along the BGH section is mainly zonal. In the subtropical domain (station S1), it is dominated by the westward flowing Agulhas Current in the upper water column ($z < 1500$ m) and at depth by the eastward transport of SE-NADW as delineated by Sokolov and Rintoul (2009). Stations S2, S3 and S4 are located within the Antarctic Circumpolar Current, flowing eastward throughout the water column. Finally station S5 is located in the Northern limb of the Weddell gyre, also flowing eastward. Therefore, the BGH section is approximately perpendicular to the climatological mean (dominant) flows, so that water masses should not flow directly from one BGH station to another. The different BGH stations would therefore not be directly connected by the mean flow. However, superimposed on this vigorous zonal circulation, slower meridional transports are clearly visible on meridional sections of water mass tracers such as salinity, temperature or nutrients, revealing notably the northward transport of AAIW and AABW, and southward transport of NADW (Abadie et al., 2017). This meridional transport is presumably a residual circulation in which lateral eddy fluxes largely balance the wind-driven circulation (Marshall and Speer, 2016). While the circulation in the BGH area is therefore clearly 3D and dominated by zonal flows (preventing a direct link by mean advection between our 5 stations), some of the BGH samples can still reflect the effect of these meridional transports of these water masses upstream of the BGH section. In the following, transport models will be used to link tracer properties measured along the BGH section. We do not assume that the transports actually act along the BGH section (pure meridional transport is not realistic). However, we use the tracer properties measured along the BGH section to elucidate and quantify the meridional component (advection, diffusion) embedded within a dominant zonal component and therefore acts upstream of the BGH section, for instance between the Drake Passage and the BGH section.

167   2.2. Sampling

168   The BONUS GoodHope cruise took place in the framework of the international polar

169   year (IPY) from February 8th 2008 till March 17th 2008 on board the Research Vessel Marion-

170   Dufresne II, from 34°S 18°E to 51°S 00°W and from 51°S to 58°S along the Greenwich

171   meridian. The expedition took place during the late austral summer, when biological activity

172   is high and ice cover is reduced. Five depth profiles (S1–S5 stations) were sampled for both

173   dissolved and particulate Th with 10 or 11 depths per profile with 1 duplicated sample at

174   stations S3, S4 and S5 (Fig. 1). An intercalibration (hereafter referred to as 'intercal') station

175   was analyzed for 3 depths which were all duplicated.

176   Seawater samples were collected using Niskin bottles equipped with Teflon coated

177   strings and mounted on a rosette frame with a CTD sensor. Challenger Oceanic *in situ* pumps

178   (ISP) were used to filter large seawater volumes through SUPOR filters (pore size: 0.45 μm,

179   filter diameter: 293 mm). Typically, volumes ranging from 200 L to 1000 L were filtered.
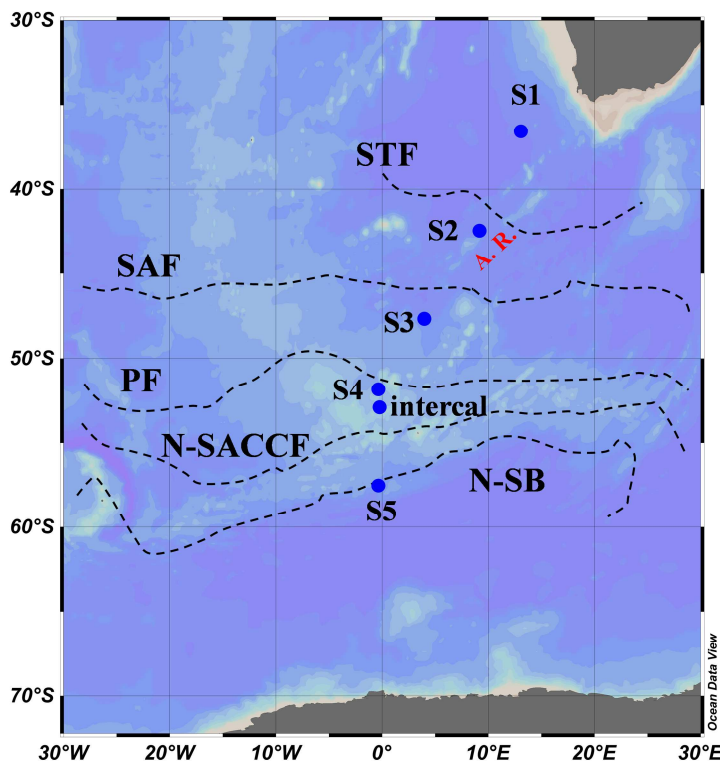
180

181   Fig. 1. Sampling stations during the BONUS-GoodHope section and main fronts (following

182   Sokolov and Rintoul, 2009; mean path position): STF = SubTropical Front; SAF = SubAntarctic Front

183   (middle branch); PF = Polar Front (middle branch); N-SACCF = northern branch of the Southern ACC

184   front; N-SB = northern branch of the Southern Boundary. A.R.: Aghulas Ridge.

185

186

6
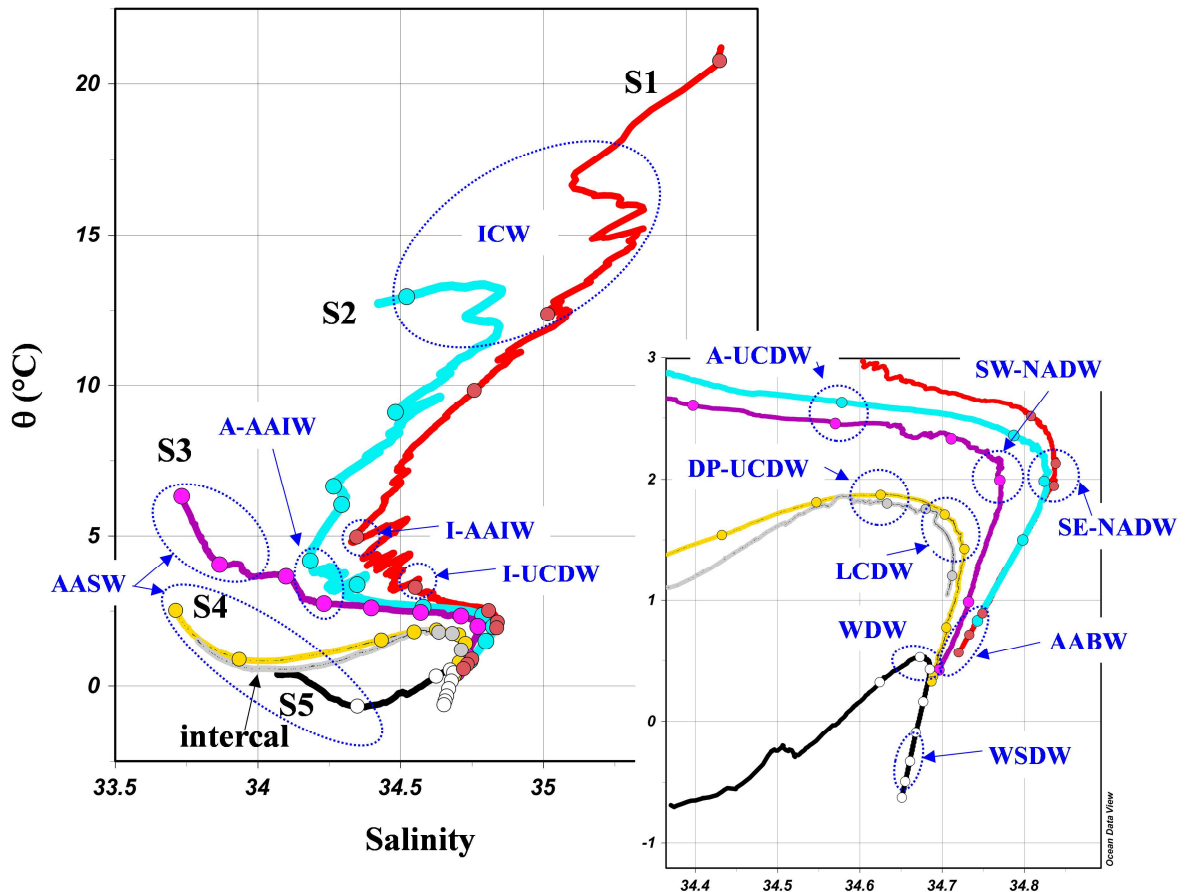
Fig.2: Potential temperature-salinity data during BGH. (a): full depth profiles. (b): deep waters. Dots: data at the depth of dissolved Th samples. Acronyms: AABW, Antarctic Bottom Water; AASW, Antarctic Surface Water; I-AAIW and A-AAIW, Antarctic Intermediate Water of Indian and Atlantic origins; I-CW, Indian Central Water; I-UCDW, A-UCDW, and DPUCDW, Indian, Atlantic, and Drake Passage Upper Circumpolar Deep Water; LCDW, Lower Circumpolar Deep Water; SE-NADW and SW-NADW, Southeast and Southwest North Atlantic Deep Water; WDW, Warm Deep Water; WSDW, Weddell Sea Bottom Water; WW, Winter Water.

2.3. Analytical procedure

Filtered seawater

Twenty liters of filtered seawater (Nuclepore, 90 mm diameter, 0.4 μm pore size) were acidified, spiked with [229]Th and pre-concentrated on board using the ferric hydroxide co-precipitation technique as described in Piepgras et al. (1979). The precipitate was then recovered on filters (Supor, 90 mm, 0.4 μm), which were kept in petri dishes and stored in the dark. Back in the laboratory, the filters were submerged in 40 mL of 6 M HCl for 24 h in 300 mL Polytetrafluoroethylene beakers, enabling the dissolution of precipitate. The filters were

7

206 then carefully rinsed with deionized water to recover all the dissolved precipitate. After

207 evaporation, the residue was dissolved in 0.5 mL 7M HNO_3 and loaded on an anion-exchange

208 column (AG1-X8 resin, 200–400 mesh) to separate the thorium fraction from the major

209 elements, uranium and the rare earth elements (REE) (adapted from Jeandel et al., 2011). The

210 total ^{232}Th chemical blank is typically 48 ± 14 pg and represents generally less than 15% of

211 the sample although peaks with 50% of the sample occur for very ^{232}Th-poor samples. Total

212 ^{230}Th chemical blank is typically 2.3 ± 0.1 fg and represents generally less than 5 % of the

213 sample although peaks with 30% of the sample occur for very shallow samples.

214

215 *Particles collected from Niskin bottle filtrations*

216   From the twenty liter seawater samples used for dissolved Th analyses (described

217 above), particulate samples were also available on the 90mm diameter 0.4µm porosity

218 Nuclepore membranes used for filtration (hereafter referred to as Niskin filtration).

219 Membranes were transferred from their petri dishes to Teflon beaker containing 15mL 6M

220 HCl and 2.5mL 15M HNO_3. They were heated 90 minutes at 130°C. After leaving them cool,

221 0.5mL 23M HF was added, and the mixture was heated again as previously. The membranes

222 were removed from the leaching solutions and rinsed over the beakers with milliQ water.

223 After evaporation, the samples were dissolved in 3mL 0.32M HNO_3 for analysis by

224 Quadrupole Induced Coupled Plasma Mass Spectrometry.

225

226

227

228 *Particles collected from in situ pump filtrations*

229   Filters from the in situ pumps were cut into pieces using ceramic scissors. Several

230 leaching steps were necessary to recover Th without attacking the filters. Filter pieces were

231 first leached with 200 mL of 6N HCl and 1.5 mL of 24-25N HF in a 300 mL Teflon beaker

232 for 2 days at 75°C. The filter pieces were removed from the leaching solution and rinsed with

233 a MQ water squeeze bottle over the leaching beaker. The filter pieces were saved apart. The

234 leaching and rinsing solutions were evaporated down to ~10 mL and transferred into a 30 mL

235 Teflon beaker. Then, the filter pieces were leached a second time with 150 mL of 7N HNO_3

236 and 0.05 mL of 29N HF for 2 days at 75°C. The filter pieces were removed from the leaching

237 solution and rinsed with MQ water that was again recovered into the leaching beaker. After

238 evaporation to a few mL, this solution was added to the first leaching/rinsing solution. The

239 300 mL Teflon beaker was rinsed in warm diluted HNO_3 to remove any particle sticking on

the beaker walls and the resulting solution was also added to the 30 mL beaker. The resulting solution was then spiked with ^{229}Th (and ^{233}Pa), dried and dissolved again in a solution with 4 mL of 14N HNO_3 and 1 mL of 12N HCl. After 1 night on a hot plate, the solution was dried and the residue was dissolved again in 10 ml of 1N HNO_3. Since filters were not rinsed immediately after filtration with distilled water on board, it was preferable to remove the salt before the column chemistry. Therefore, 40µL of a Fe solution (60 mg/g) were added. After 1h-heating, Fe was precipitated by raising the pH to about 8 with NH_3. The Fe precipitate (that coprecipitates Th isotopes) was separated by centrifugation and rinsed several times. Finally, it was dissolved in 0.25 ml of 8N HNO_3, ready for loading on an anionic column. Th isotopes were separated from Fe by ion exchange chromatography on a small volume (0.5 ml) column of AG1X8 resin (200-400 mesh) with a procedure adapted from Jeandel et al., 2011 (Gdaniec et al., 2018).

The total ^{232}Th chemical blank was typically 42 ± 25 pg, although few blanks as high as 1400 pg were observed. Given the good agreement between the particulate ^{232}Th concentrations obtained with the Niskin filtrations (see Fig. ES1) and the ISP ^{232}Th concentrations corrected with the low blank values, the highest blanks were not taken into account to correct the ISP data. Total ^{230}Th chemical blank was typically 1 ± 1 fg. As for ^{232}Th, a small number of very large blanks (up to 125 fg) were obtained but assumed to be outliers.

Mass spectrometry

For dissolved and in situ pump samples, Th isotopes were measured on a MC-ICPMS Neptune + (Thermo-Fischer). The dissolved samples were analyzed with the initial configuration of the Neptune + with an Apex desolvator. The particulate samples were analyzed after the Neptune's upgrade with a Jet interface and an Aridus 2 desolvating nebulizer. The acquisition conditions are given in Gdaniec et al. (2018). The accuracy of the MC-ICPMS measurement was checked by analysis of Th standard IRMM035 (^{230}Th/^{232}Th = (11.31±0.12)×10^{-6}, n=6) and IRMM036 (3.059±0.033)×10^{-6}, n=8), in good agreement with reference values: ^{230}Th/^{232}Th = (11.38±0.10)×10^{-6} for IRMM035 and ^{230}Th/^{232}Th = (3.047±0.024)×10^{-6} for IRMM036 (Sims et al., 2008). The quality of the analyses was checked through the GEOTRACES intercalibration exercise where we obtained precise and accurate dissolved Th concentrations well within the consensus values (Anderson et al., 2012).

274

275   For Niskin filtration samples, ^{232}Th was analyzed by quadrupolar ICPMS (Agilent

276   7500CE of the Observatoire Midi Pyrénées, Toulouse). Indium and rhenium (100 ppt, added

277   to the samples) were used as internal standards to monitor instrument sensitivity variations.

278   Reproducibility calculated from 3 duplicated samples (2 different Niskins) was on average

279   12% (2 standard deviations). Detection limit was 0.5 pg/kg.

280

281

282

283   3. Results

284   3.1. Dissolved thorium

285

286   Dissolved ^{232}Th concentrations (^{232}Th$_d$) range from 4.7 pg/kg to 288 pg/kg (Fig. 2a, Tab. ES

287   1) and generally increase with depth. At stations S1 and S2, the ^{232}Th$_d$ profiles have a local

288   maximum around 200-400 m depth and a sharp increase at bottom depths. Conversely, at

289   station S3, ^{232}Th$_d$ for the deepest sample is relatively low. This feature was also noted for

290   dissolved REE (Garcia-Solsona et al. 2014) and for ^{230}Th$_d$ (see below) analyzed on the same

291   water sample. Along the section, the lowest ^{232}Th$_d$ are found at station S3 and S4, far from the

292   coasts of Africa and Antarctica (^{232}Th$_d$ = 4.7-30 pg/kg). All the ^{232}Th$_d$ duplicates agree within

293   analytical uncertainties.

294

295
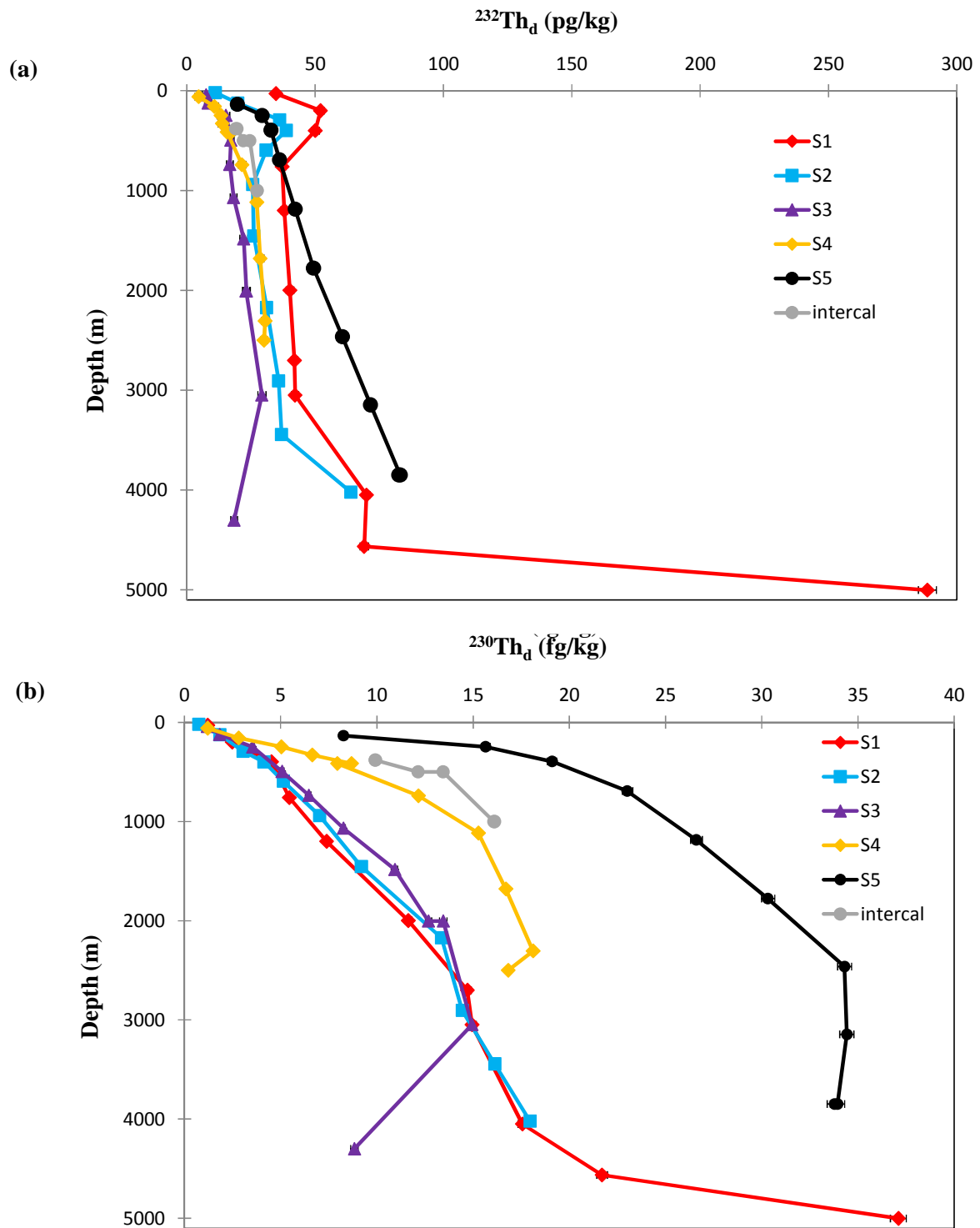
Fig. 3. Dissolved thorium profiles. a: dissolved ^{232}Th. b: dissolved ^{230}Th.

302

303

304   Dissolved ^{230}Th concentrations (^{230}Th$_d$) range from 0.7 fg/kg to 37 fg/kg (Fig. 3b) and

305   generally increase with depth. At stations S1 and S2, the ^{230}Th$_d$ profiles increase

306   approximately linearly from the surface down to 4000 m depth. At station S1, there is a sharp

307   increase of ^{230}Th$_d$ above the seafloor. Conversely, at station S3, S4 and S5, the ^{230}Th$_d$ profiles

308   have concave shapes and, for a given depth, ^{230}Th$_d$ is higher at stations S4 and S5 than at S1,

309   S2 and S3. All ^{230}Th$_d$ duplicates agree within 9% (3 of them agreeing within the analytical

310   uncertainties).

311   Following GEOTRACES good practices, a comparison with 2 stations of the Zero-Drake

312   cruise (Rutgers van de Loeff et al., 2016) is provided (Fig. ES3). Profiles agree within

313   uncertainties for ^{230}Th and more qualitatively for ^{232}Th.

314

315

316   3.2. Particulate thorium

317   Particulate ^{232}Th concentrations (^{232}Th$_p$) have been already reported elsewhere (Garcia-

318   Solsona et al., 2014). ^{232}Th$_p$ from ISP filtrations range from 0.08 pg/kg to 371 pg/kg (Fig. 4a,

319   Tab. ES2). There is generally a good agreement between ^{232}Th$_p$ profiles obtained with in situ

320   pumps and profiles obtained with Niskin filtrations. The most notable exception is above the

321   seafloor at station S3, where Niskin bottle filtration gives ^{232}Th$_p$ = 27 pg/kg, whereas ISP

322   filtration gives ^{232}Th$_p$ = 2.5 pg/kg. Apart from this particular feature recorded at S3, the ^{232}Th$_p$

323   profiles generally increase with depth with a sharp increase above the seafloor. Along the

324   section, the highest ^{232}Th$_p$ concentrations are found at station S1 and S2, which are the

325   stations closest to the African coast.

326   All the ^{232}Th$_p$ duplicates agree within analytical uncertainties. The variation in ^{232}Th$_p$

327   observed between in situ pumps and Niskin filtrations (Fig. ES1) is of the same order than

328   observed for other insoluble elements (Planquette and Sherrell, 2012).

329

330

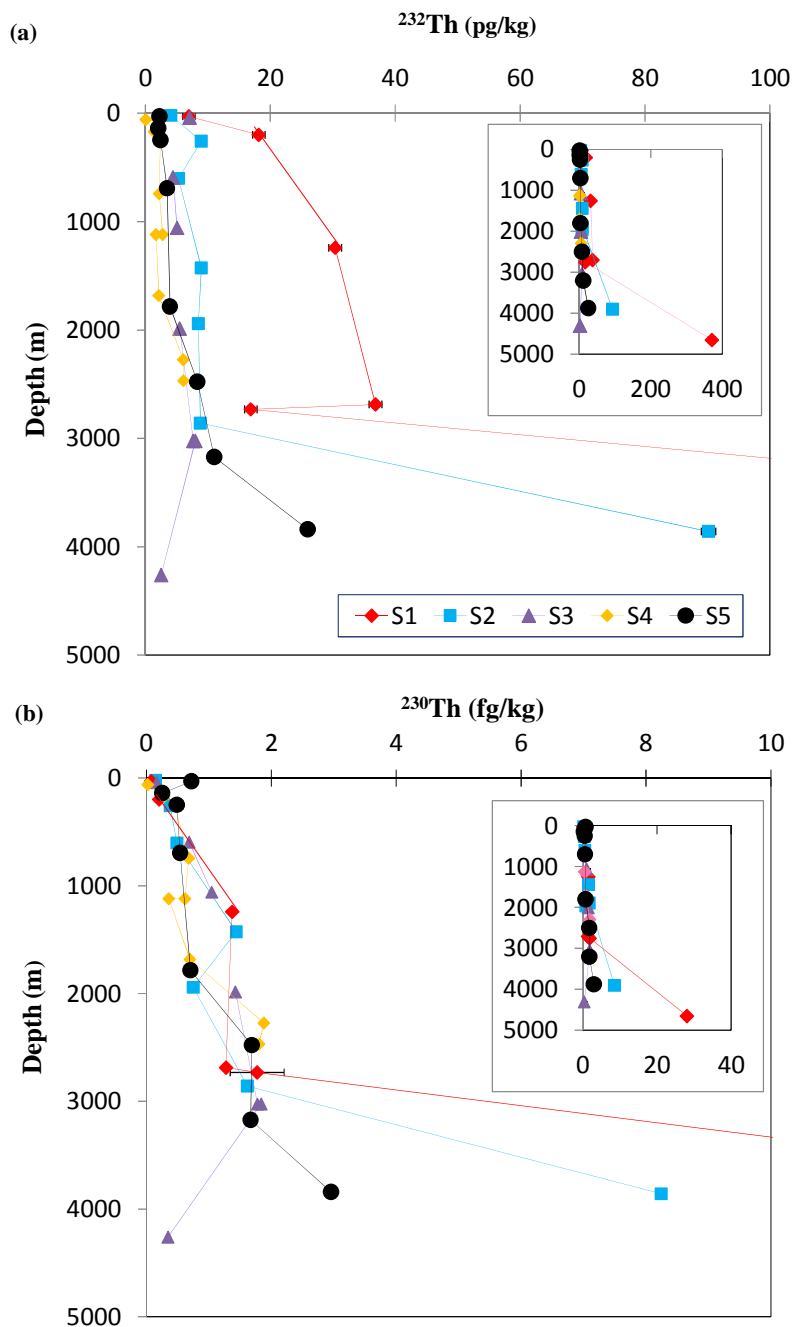331   Particulate ^{230}Th concentrations (^{230}Th$_p$) range from 0.02 fg/kg to 28 fg/kg (Fig. 4b). ^{230}Th$_p$

332   generally increase with depth. At stations S1 and S2, the ^{230}Th$_p$ profiles increase

333   approximately linearly from the surface down to 4000 m depth and then present a sharp

334   increase of ^{230}Th$_p$ above the seafloor (height above the seafloor is 295 m and 212 m at,

335   respectively, S1 and S2). At station S3, $^{230}Th_p$ decreases just above the seafloor similarly to

336   $^{232}Th_d$ (height above the seafloor is 218 m at S3).

337   Two in situ pump filtrations were replicated. At station S3 and 3050-m depth, the

338   replicates agree within 4% for both $^{232}Th_p$ and $^{230}Th_p$. At station S4 and 1130-m depth, both

339   the $^{232}Th_p$ and $^{230}Th_p$ concentrations differ by a factor of ~2, suggesting either a problem of

340   volume measurement, data recording or a loss of particles during the filter handling. We

341   choose to use the concentrations measured on the filter with the largest filtered volume of

342   water, because it corresponds to the $^{232}Th_p$ concentration closest to the Niskin filtration.

343

344

Fig. 4. Particulate Thorium profiles collected with *in situ* pumps. (a) Particulate ^{232}Th. (b) Particulate ^{230}Th. Insets: expanded concentration scales to display particulate concentration maximum at S1.

4. Discussion

4.1. ^{230}Th profiles

The dissolved ^{230}Th profiles obtained during Bonus GoodHope are consistent with previous results from the South Atlantic and the Weddell Sea (Rutgers van der Loeff and

14

355   Berger, 1993, Rutgers van der Loeff et al., 2016). Station S1 has a relatively linear profile

356   from the surface down to 3000 m deep. This is consistent with the 1D reversible scavenging

357   model, in which ^{230}Th is only transported vertically by reversible scavenging on settling

358   particles. However, even though S1 is located in the subtropical gyre, north of the subtropical

359   front, the profile is not perfectly linear. This presumably reflects the influence of surface and

360   intermediate waters advected from the Indian Ocean (ICW and AAIW down to ~1200 m) and

361   deep water advected from the Atlantic Ocean (SE-NADW). The ^{230}Th content of the surface

362   and intermediate waters at S1 compare well with those reported in the south Indian Ocean

363   (^{230}Th ≈ 4-5 fg/kg at 500 m, Thomas et al., 2006). The ^{230}Th contents of deep waters (^{230}Th ≈

364   13 fg/kg at 2000 m) at S1 are on the low side of those reported for SE-NADW sampled off

365   Namibia (^{230}Th ≈ 12-24 fg/kg at 2000 m, Scholten et al. 2008) and that flows towards S1

366   (Arhan et al., 2003), suggesting the imprint of boundary scavenging. The deepest parts of the

367   S1 profile significantly deviate from the linear increase: the higher dissolved and particulate

368   ^{230}Th (as well as ^{232}Th) concentrations suggest a release from the South African margin

369   sediments.

370   From the surface down to 3000 m depth, the ^{230}Th profiles of S2 and S3 are similar to

371   S1. In the deepest waters, S2 has a strong increase of its dissolved and particulate ^{230}Th

372   (although less than S1) also suggesting inputs from the sediments or lateral transport from the

373   African margin. By contrast, at S3, the low ^{230}Th$_d$ concentrations at a depth of 4500 m could

374   also be attributed to bottom scavenging (a low REE content on the same sample was also

375   noted by Garcia-Solsona et al., 2014).

376   The strongly concave shapes of the ^{230}Th$_d$ profiles at S4 and S5 strongly suggests these

377   profiles are impacted by the upwelling of LCDW (Rutgers van der Loeff and Berger, 1993).

378   The ^{230}Th$_d$ profile at S3 has also a concave shape that can be regarded as a result of the

379   LCDW upwelling. However, above 3000 m depth, it is not so different from the S1 profile

380   where no LCDW upwelling is suspected. Also, the low ^{230}Th$_d$ concentrations at a depth of

381   4500 m, that accentuate the nonlinearity of the profile, could also be attributed to bottom

382   scavenging.

383

384   At stations S1, S2 and S3, the ^{230}Th$_p$ profiles have very similar slopes, particularly from the

385   surface down to 1500 m depth. We consider the conservation equation of the 1D reversible

386   scavenging model at steady state (and neglecting ^{230}Th radioactive decay):

387         $\frac{\partial C_t}{\partial t} = P_d - w_p \frac{\partial C_p}{\partial z} = 0$ (2)

388   Where C_t is the total (dissolved + particulate) ^{230}Th concentration, P_d is the in situ production

389   rate of ^{230}Th ($P_d = 0.56$ fg/kg/y), w_p is the particle settling speed and C_p the particulate ^{230}Th

390   concentration. Hence, w_p is given by: $w_p = P/(\partial^{230}Th_p/\partial z)$. Using an average slope of 0.001

391   fg/kg/m, we obtain that $w_p = 560$ m/d, in agreement with Rutgers van der Loeff and Berger

392   (1993).

393

394

395   In the southern part of the section, we first use the mixing-scavenging model

396   introduced by Rutgers van der Loeff and Berger (1993) to evaluate the impact of lower

397   Circumpolar Deep Water upwelling and input into the Weddell Gyre. This "scavenging-

398   mixing" model relies on several assumptions:

399   (i) The representation of mixing with a constant restoring term at all depths (eq. 3). This is

400   largely ad hoc, so that the physical interpretation of C_{it} and τ_w is unclear.

401   (ii) the omission of the effects of vertical transport by advection and diffusion,

402   (iii) steady state,

403   (iv) the partition coefficient K is vertically uniform. It implies that the ^{230}Th$_{xs}$ particulate

404   fraction is constant over the depth profile. Clear variations of the ^{230}Th$_{xs}$ particulate fraction

405   (Tab. ES2) occur in the deepest samples either due to particle inputs from the margins

406   (stations S1, S2 and S5, see Gdaniec et al., 2019) or following hydrothermal scavenging

407   (station S3).

408   (v) K is very small compared to 1, so that C_d could be approximated by C_t. Apart for the

409   deepest samples at stations S1 and S2, it introduces an underestimation of w_p by 13 % at most.

410   (vi) the particle settling velocity w_p is vertically uniform. This assumption is deduced the from

411   linear dissolved and particulate ^{230}Th profiles observed in regions unaffected by strong deep

412   currents (Roy-Barman et al., 1996).

413   (vii) C_d is negligible near the surface.

414

415   Using the above assumptions, the tracer conservation equation of this model is:

16

416

$$\frac{\partial C_t}{\partial t} = P_d + \frac{(C_{i\_t} - C_t)}{\tau_w} - w_p \frac{\partial C_p}{\partial z} = 0 \qquad (3)$$

418 Where τ_w is restoring time scale taken equivalent to the water residence time and C_{i_t} is the

419 total ^{230}Th concentration of the inflowing water. Introducing a partition coefficient between

420 dissolved and particulate Th, $K = C_p / C_d$ and integrating equation 3 vertically over the water

421 column, the ^{230}Th$_d$ concentration at any depth is given by:

$$C_d = \left(C_{i\_t} + P_d \tau_w \right) \times \left(1 - \exp \left(-\frac{z}{w_p K \tau_s} \right) \right) \qquad (4)$$

423

424 For station 5, we use the ^{230}Th$_i$ = 24 fg/kg for the LCDW (Rutgers van der Loeff and Berger,

425 1993), K=0.04 is the average ratio measured at this station. Then, we adjust w_p = 875 m/y and

426 τ_w= 20 y to obtain a good agreement between the modelled curve and the data (Fig. 5). The

427 low τ_w obtained here compared to 45 y used by Rutgers van der Loeff and Berger (1993)

428 derives presumably from the relatively peripheral position of station S5 in the Weddell Sea.

429 We confirm that the scavenging residence time in the Weddell Sea (τ_s=d/(2Kw_p) = 55 y for a

430 water column of a depth of d = 4000 m) is larger than in the subtropical gyre (τ_w = 25 y for a

431 water column of a depth of 4000 m). On the whole, the model explains why the ^{230}Th$_d$

432 concentrations are high and do not increase linearly with depth in the Weddell Gyre.

433 We apply the same model to station S4. Here ^{230}Th$_i$ is also adjusted to obtain a good

434 data-model agreement. We note that 2 modeled curves based on relatively different sets of τ_w

435 and w_p values (ACC high and ACC low, Fig. 5) agree with the S4 data. This illustrates a limit

436 of this method to estimate particle settling velocities.

437

438
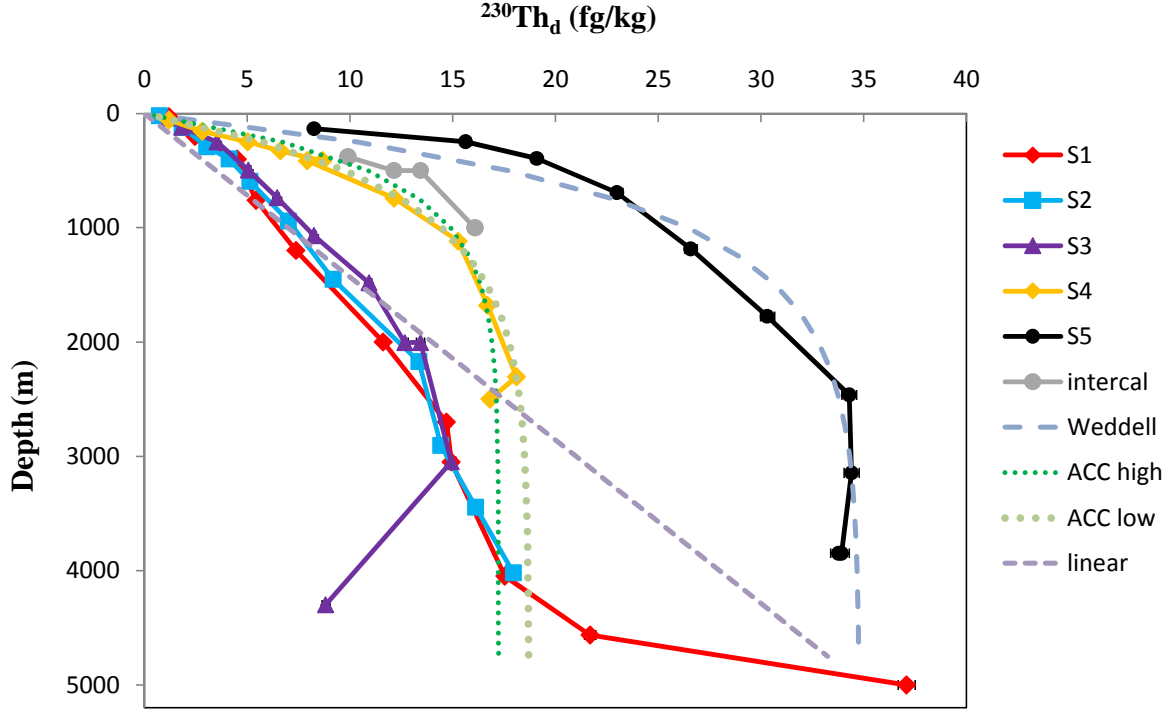
Fig. 5. Modelling of the Bonus Good Hope profiles. The dotted and dashed curves are calculated with Eq. 4. Weddell: $C_i = 24$ fg/kg, $w_p = 875$ m/y, $\tau_w = 20$ y and $K = 0.04$. ACC low: $C_i = 12$ fg/kg, $w_p = 803$ m/y, $\tau_w = 12$ y and $K = 0.07$. ACC high: $C_i = 15$ fg/kg, $w_p = 1785$ m/y, $\tau_w = 4$ y and $K = 0.125$. linear: $C_i = 0$ fg/kg, $w_p = 800$ m/y, $\tau_w = +\infty$ and $K = 0.1$.

This advection-scavenging model has been largely used to describe the vertical distribution of ^{230}Th in the Southern Ocean (Coppola et al., 2006, Venchiarutti et al., 2011, Rutgers van der Loeff et al., 2016). Despite crude assumptions (e.g., uniform influence throughout the water column by a single water mass), this mixing-scavenging model has the great merit of highlighting the impact of upwelling on ^{230}Th$_d$ profiles and to provide an estimate of the particle settling speed when the 1D production-scavenging model cannot be used. Nevertheless, this model cannot fully describe the upwelling and mixing of 2 different water masses along an isopycnal surface as observed during BGH and described in the next section. Salinity data help to illustrate this point. For a conservative tracer ($P_d = 0$, $w_p = 0$ and $C_p = 0$) and assuming steady state, equation (3) reduces to:

$$\left(S_{t\_i} - S_t\right) = 0 \tag{5}$$

This expresses that salinity is constant and equal to the salinity of the inflowing water ($S_t = S_{t\_i}$). In this model, LCDW is advected at all levels in the Weddell Gyre. It implies that the Weddell Gyre must be filled only with LCDW. Nevertheless, the ^{230}Th$_t$ concentration in the

Weddell Gyre changes with depth due to the scavenging transport of ^{230}Th$_t$ by sinking particles. Hence, this mixing-scavenging model cannot represent the mixing of water masses with different origins and labeled with different θ and S signatures as they are observed along the BGH section and elsewhere in the Southern Ocean. In principle, general circulation models, associated or coupled with biogeochemical model, have the potential to reproduce the coupled effect of scavenging and mixing, but the present generation of coupled models do not accurately describe the vertical distribution of scavenging intensity (e.g.: Dutay et al., 2009, Gu and Liu, 2017, Van Hulten et al., 2018).

4.2. Th isotopes along neutral density surfaces

While there are large horizontal concentration gradients of ^{230}Th$_d$ and total (dissolved + ¨particulate) ^{230}Th (^{230}Th$_t$) along the BGH section (mostly between station S3 to S5, Fig 3), ^{230}Th$_t$ concentration gradients are small on a given neutral density surface (Fig. 6). Figure 6 highlights that distribution of ^{230}Th$_d$ is mainly driven by transport from upwelling and mixing along isopycnal surfaces. There is more variability of ^{232}Th$_d$ or ^{232}Th$_t$ (dissolved + particulate ^{232}Th) on a given neutral density value, presumably because large lithogenic inputs occur at stations S1 and S2 (Fig. 6).
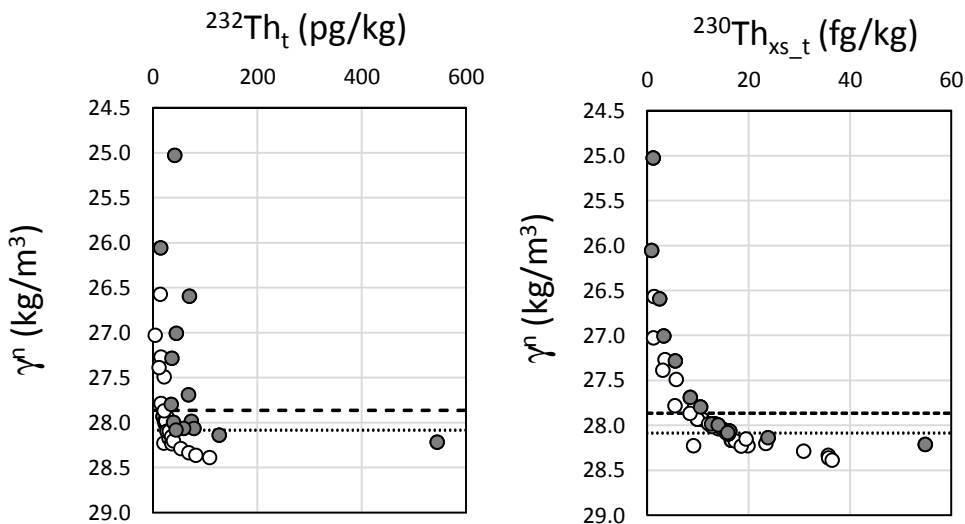
Fig. 6. Neutral density versus ^{232}Th$_t$ and ^{230}Th$_t$ concentration. Grey dots: S1 and S2 stations with high ^{232}Th$_t$ contents. White dots: S3, S4 and S5. Dashed line: γ^n = 27.865 kg/m^3. Dotted line: γ^n = 28.094 kg/m^3.

484   In the following, we discuss concentration changes along isopycnal surfaces. As these
485   changes are small, we restrict this discussion to the Bonus GoodHope data, all generated in
486   the same laboratory, in order to avoid the systematic inter-laboratory differences identified
487   during the GEOTRACES intercalibration (Anderson et al., 2012).

488   We focus on 2 neutral density surfaces: $\gamma^n = 27.865$ kg/m^3 and $\gamma^n = 28.094$ kg/m^3 (Fig
489   ES2). The neutral density surface $\gamma^n = 27.865$ kg/m^3 can be followed from z=1500 m at
490   station S1 to z=139 m at station S5. It crosses the following water masses: I-UCDW (S1), A-
491   UCDW (S2 and S3), DP-UCDW (S4) and AASW/WW (S5). The neutral density surface: $\gamma^n =$
492   28.094 kg/m^3 can be followed from z = 3000 m at station S1 to z = 200 m at station S5. It is
493   close to the neutral density of the deep salinity maximum observed in 2004 along the same
494   section (Gladyshev et al., 2008). It crosses the following water masses: SE-NADW (S1 and
495   S2), SW-NADW/AABW (S3), LCDW (S4) and AASW/WW (S5).

496

497   We choose these two neutral density surfaces because: (1) they are found along the whole
498   section, (2) samples along these surfaces tend to form a linear trend on a θ-S diagram,
499   indicating a binary mixing (Fig. 7), and (3) they are not interrupted by the Agulhas Ridge.
500   When, at a given station, no sample was collected exactly on the selected neutral density
501   surface, concentrations were linearly interpolated between the samples collected just above
502   and below this surface at the same station. When the particulate Th was not analyzed with *in*
503   *situ* pump samples at the target depth or in its vicinity (e.g., intercal station), we used the
504     $^{232}Th_p$ concentration obtained with the Niskin filtration profiles and the $^{230}Th_p$ was calculated
505   with the ($^{230}Th_p/^{232}Th_p$) ratio linearly interpolated between the ratios measured on particles
506   just above and below or at the nearby station:

507     $$^{230}Th_{p\text{-estimates}} = {}^{232}Th_{p\text{-Niskin filtration}} * ({}^{230}Th_p/{}^{232}Th_p)_{\text{interpolated}} \qquad (6)$$

508

509   <u>$\gamma^n = 27.865$ kg/m^3</u>

510   On a θ-S diagram, S1, S2, S3 and S4 plot along a straight line, suggesting a binary mixing
511   between S1 and S4 (Fig. 7a). S5 does not fall on this line, possibly due to ocean-atmosphere
512   interactions (Abadie et al., 2017), so that this station does not correspond to the same binary
513   mixing along this neutral density surface. Therefore, in the following, we will apply the
514   mixing model mostly between stations S1 and S4 for this isopycnal.
515   On a S- $^{232}Th_t$ diagram, the stations S3, S4 and intercal stand below the conservative mixing
516   line between S1 and S4 (Fig. 7c). It corresponds to a depletion (net removal of ^{232}Th on

517   sinking particles) of $^{232}Th_t$ compared to a conservative mixing between S1 and S4: $\Delta^{232}Th_t<0$.

518   The strong $^{232}Th_t$ inputs from the South African margin to the ACC are marked by a strong

519    $^{232}Th_t$ concentration gradient ($^{232}Th_t$ decrease by a factor ~4 between stations S1 and S4). A

520   small $^{232}Th_t$ gradient between Station S5 and S4 suggests smaller inputs from the Weddell

521   Sea.

522

523   On a S- $^{230}Th_t$ diagrams, there is much less change in $^{230}Th_t$ concentration (~ 30% between

524   stations S1 and S4) compared to $^{232}Th_t$ presumably because the margin is not a strong source

525   of $^{230}Th_t$ for the ACC. Nevertheless, the $^{230}Th_t$ concentrations generally decrease southward.

526   However, stations S2 and S3 stand above the conservative mixing line between S1 and S4

527   (Fig. 7e). This trend would correspond to an excess of $^{230}Th_t$ compared to a conservative

528   mixing between S1 and S4: $\Delta^{230}Th_t>0$. There is an accumulation of ^{230}Th due to *in situ*

529   production despite the net removal of $^{232}Th_t$ during the same mixing process.

530

531   <u>$\gamma^n =28.094$ kg/m^3</u>

532   On a θ-S diagram, S3, S4, intercal and S5 plot along a straight line, suggesting a

533   binary mixing between S3 and S5 (Fig. 7b). S1 and S2 do not fall on this line, so that these 2

534   stations do not correspond to the same binary mixing along this neutral density surface.

535   Therefore, in the following, we will restrict our analysis to stations S3 to S5 and, in the next

536   section, we will apply the mixing model only between stations S3 and S5.

537   On a S-$^{232}Th_t$ diagram, we observe the same trend as on the previous isopycnal: a

538   strong $^{232}Th_t$ decrease from S1 to S3 and a weaker decrease from S5 to S4 (Fig 7d). This

539   illustrates the role of the margins (and particularly the South African margin) as sources of

540   ^{232}Th for the ACC. We argued in the previous paragraph that waters from stations S1 and S2

541   do not seem directly involved in the mixing observed further south. However, high $^{232}Th_t$

542   concentrations are also observed in the SW-NADW sampled upstream of the BGH section.

543   These high values are acquired as this water flows along the Namibian margin (Scholten et

544   al., 2008) so that it could be a suitable $^{232}Th_t$ source fueling the southern part of the BGH

545   section. S4 and intercal stations stand below the S3-S5 binary mixing line, reflecting $^{232}Th_t$

546   depletion at these 2 stations compared to conservative mixing, expressed as $\Delta^{232}Th_t<0$ (Fig 7).

547   More generally, paired $^{232}Th_t$–S data indicates that there is a net Th removal by the settling

548   particles while water masses mix between stations S3 and S5.

549

550 As for $\gamma^n = 27.865$ kg/m^3, the relative variations of ^{230}Th$_t$ are small (Fig. 7f). On a S-

551 ^{230}Th$_t$ diagram, the S4 and intercal stations stand above the S3-S5 binary conservative mixing

552 trend (S1 and S2 are not considered because they are not involved in the mixing on this

553 isopycnal). This trend would correspond to an excess of ^{230}Th$_t$ compared to a conservative

554 mixing: Δ^{230}Th$_t > 0$. Like on the previous isopycnal, ^{230}Th accumulates due to *in situ*

555 production despite the net removal of ^{232}Th$_t$ during water mass mixing.
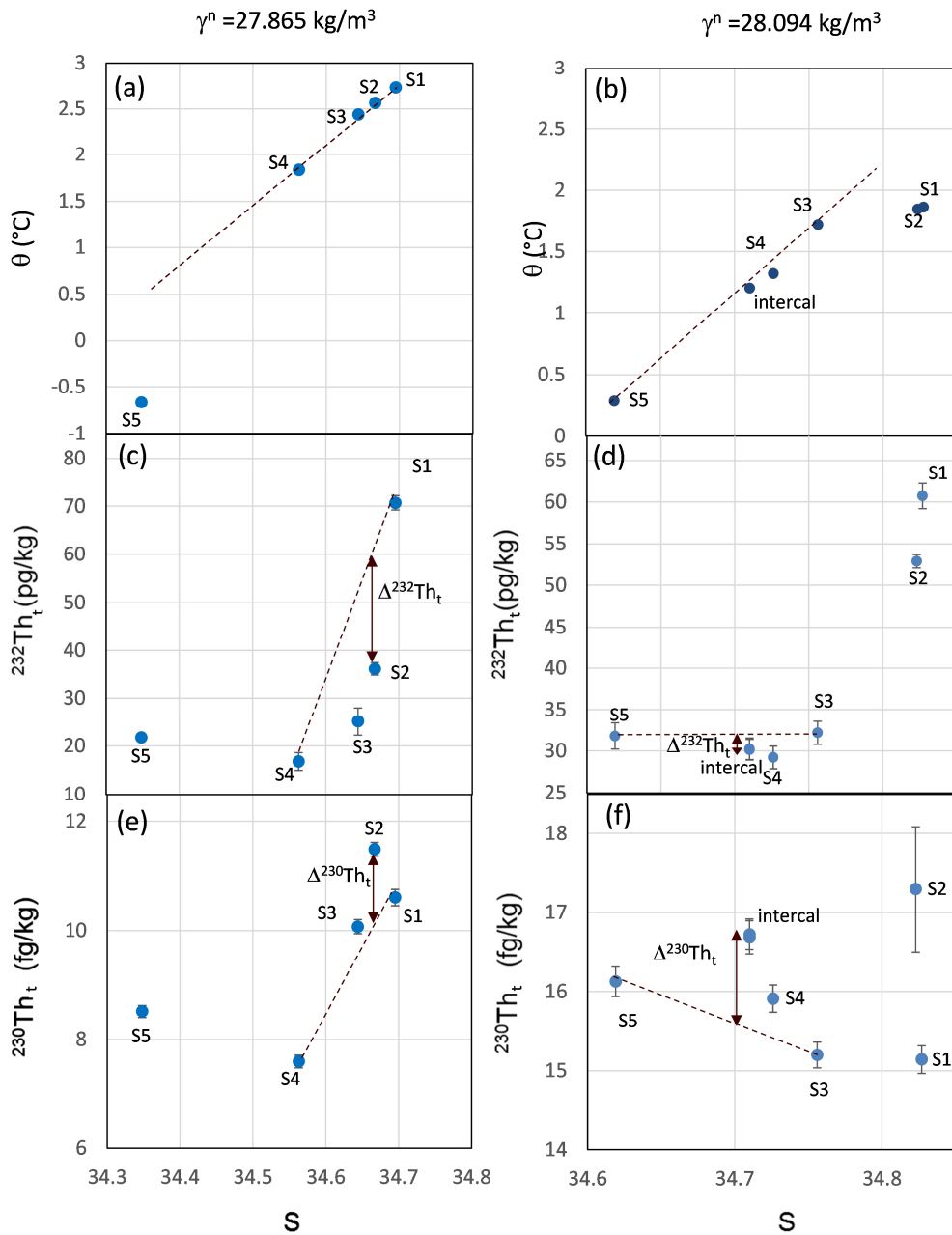
556
557 Figure 7: Potential temperature, ^{232}Th$_t$ and ^{230}Th$_t$ versus salinity on different neutral density surfaces.

558 Left: $\gamma^n = 27.865$ kg/m^3. Right: $\gamma^n = 28.094$ kg/m^3. a-b: Potential temperature versus salinity. c-d: ^{232}Th$_t$

559   versus salinity. e-f: ^{230}Th$_t$ versus salinity. Thin dashed line: conservative binary mixing line. Vertical

560   double arrows denote the deviation compared to conservative mixing.

561   See table ES3 for the data calculated on isopycnals.

562

563   4.3. Modeling advection-diffusion-scavenging along a neutral density surface.

564   In the deep ocean, water mass mixing is thought to occur preferentially along

565   isopycnal surfaces. There is both advection and eddy diffusion along the steep isopycnal

566   surfaces of the Southern Ocean (Zika et al., 2009, Naveira Garabato et al., 2007). While

567   diapycnal mixing is important in the Drake Passage due to the rough topography, it appears to

568   be much weaker out of the passage (Watson et al., 2013), so we will neglect it for the present

569   analysis. We approximate the combined effect of advection and diffusion along an isopycnal

570   by extending the conservation equation (2) with the explicit introduction of advection and

571   diffusion terms in an infinitesimal volume of water at steady state (Jenkins, 1987):

572     $K_i \frac{\partial^2 C_t}{\partial x^2} - u_i \frac{\partial C_t}{\partial x} + P_d - w_p \left(\frac{\partial C_p}{\partial z} \right) = 0$ (7)

573   Where C_t is the total (dissolved + particulate) concentration of the tracer, C_p the particulate

574   concentration of the tracer, K_i is the cross-stream isopycnal eddy diffusion coefficient and u_i

575   is the cross-stream isopycnal advection velocity. The x-axis is parallel to the isopycnal surface

576   in the meridional direction and oriented northward. The z axis is oriented perpendicular to the

577   isopycnal surface and hence is almost vertical. Just like in the advection-scavenging model

578   (equ. 3), keeping w_p out of the partial derivative with respect to z (writing $w_p \left(\frac{\partial C_p}{\partial z} \right)$ instead of

579     $\left(\frac{\partial (w_p C_p)}{\partial z} \right)$) requires to assume that w_p does not vary with z. We integrate Eq. 7 along

580   isopycnal surfaces of the BGH section between the stations corresponding to the end members

581   of water mass mixing (stations for S1 and S4 for γ^n =27.865 kg/m^3 and S3 and S5 for γ^n

582   =28.094 kg/m^3). Unlike most Th models that are built by vertically integrating the

583   conservation equation, here we integrate the conservation equation along surfaces that are

584   only slightly tilted relative to the horizontal. This is a simplified view of water transport

585   because while water moves across the ACC, it is also rapidly advected eastward by the ACC

586   (S2-S4) and the northern limb of the Weddell Gyre (S5). We assume that K_i, u_i, w_p and

587   (dC$_p$/dz) are all constant along x in order to obtain analytical solutions. We note $C_t = C_{t-conc} +$

588   ΔC_t, where C_{t-conc} is the concentration of the tracer if it had a conservative behavior and ΔC_t

589   (as plotted in Fig 7) is the deviation of this tracer compared to a conservative behavior. The

590   solution is then:

591

$$C_{t-conc} = \frac{e^{\frac{u_i}{K_i}x} - e^{\frac{u_i}{K_i}x_B}}{e^{\frac{u_i}{K_i}x_A} - e^{\frac{u_i}{K_i}x_B}}\left(C_{t\_A} - C_{t\_B}\right) + C_{t\_B} \tag{8}$$

592

$$\Delta C_t = \frac{\left(P_d - w_p\frac{dC_p}{dz}\right)}{u}\left((x - x_B) + (x_B - x_A)\left(\frac{e^{\frac{u_i}{K_i}x} - e^{\frac{u_i}{K_i}x_B}}{e^{\frac{u_i}{K_i}x_A} - e^{\frac{u_i}{K_i}x_B}}\right)\right) \tag{9}$$

593

594

595

Here A and B represent stations S1 and S4 or S3 and S5 along the neutral density surface. For

596

a conservative tracer such as salinity, the concentration is given by:

597

$$S = \frac{e^{\frac{u_i}{K_i}(x - x_A)} - 1}{e^{\frac{u_i}{K_i}(x_B - x_A)} - 1}\left(S_B - S_A\right) + S_A \tag{10}$$

598

599
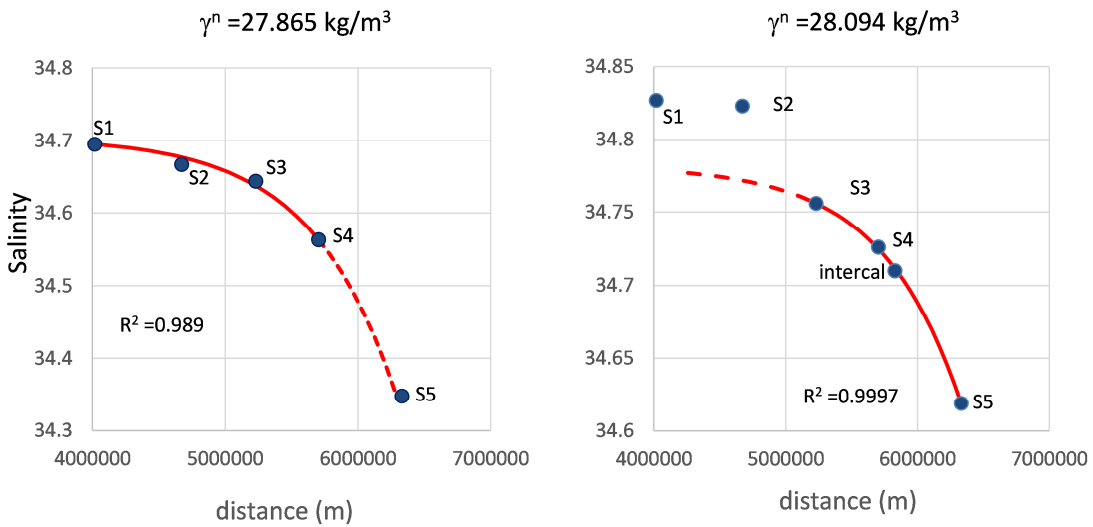
Figure 8: Advection-diffusion modelling of salinity. The distance considered is the meridian distance

602

from the equator (d = 0 at the equator). Red curves are obtained with equation 10. u_i/K_i is adjusted by

603

least squares just based on the stations corresponding to the 2-water mass values of u_i/K_i are mixing

604

and by forcing the curves to pass through the 2 water mass end members. The values of u_i/K_i are given

605

in Table 1. Dotted curves are extrapolated to the rest of the section but the corresponding stations are

606

not used to calculate the curve parameters.

607

608

609

610

611

γ^n =27.865 kg/m^3

γ^n =28.094 kg/m^3

612
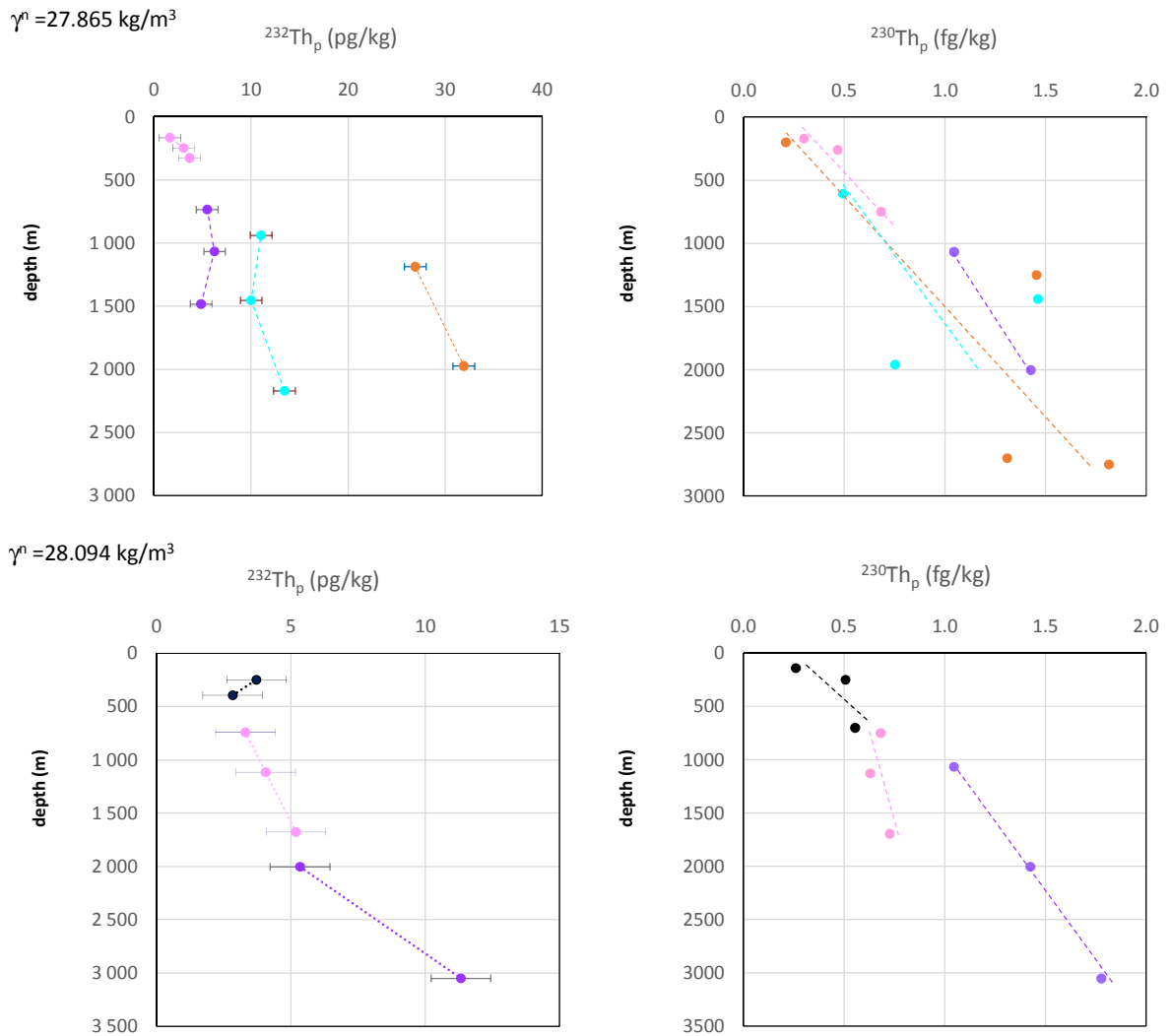
Figure 9: ^{232}Th$_p$ and ^{230}Th$_p$ profiles. For each isopycnal, we also plot the sample analyzed just above
and below in order to define the slopes (d^{232}Th$_p$/dz) and (d^{230}Th$_p$/dz), respectively. Color code is the
same as in Figure 3.

616

617

618    $\underline{\gamma^n = 27.865}$ kg/m^3

619   Equation 10 allows determining the u_i/K_i ratio using salinity data along the BGH

620   section. For $\gamma^n = 27.865$ kg/m^3, we obtain $u_i/K_i = - 1.57 \times 10^{-6}$ m^{-1} (Fig. 8, Tab. 1). The minus

621   sign corresponds to a southward advection ($u_i < 0$ and K_i is always positive). This is consistent

622   with the southward upwelling expected based on the average circulation of UCDW in the

623   Southern Ocean within this density range (section 2.1). This feature is observed for the 2

624   isopycnals studied here (see below for $\gamma^n = 28.094$ kg/m^3).

625

626
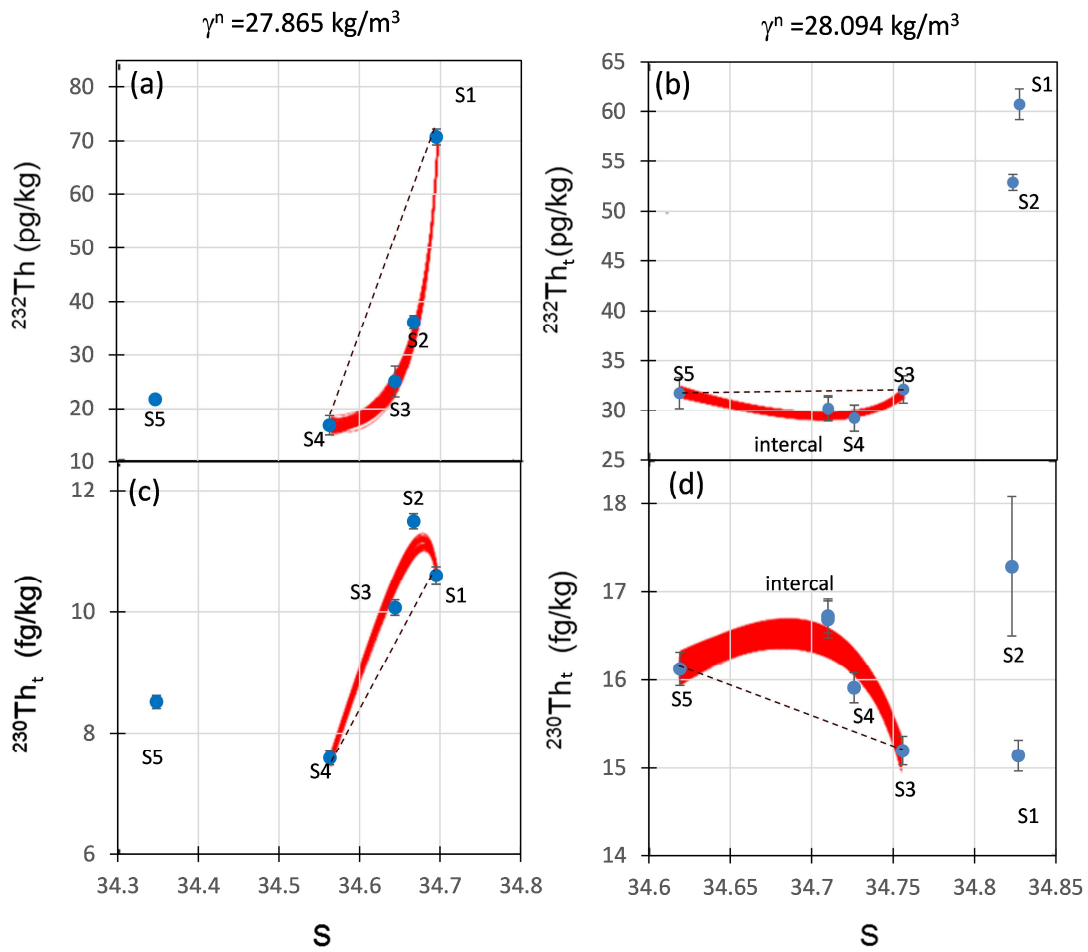
627

628   Figure 10: Advection-diffusion modelling of S and Th_t isotopes compared to data. Staked red

629   curves: modelled curves with the highest R^2 values (Tab. 1). Thin black dotted line:

630   conservative mixing between S3 and S5.

631

632

633   Tab. 1: Model parameters and outputs.

	$d^{232}Th_p/dz$ (pg/kg/m)	$d^{230}Th_p/dz$ (fg/kg/m)	u_i/K_i (m^{-1})	K_i (m^2/s)	u_i (m/s)	w_p (m/y)	R^2_0	R^2_2
$\gamma^n = 27.865$ kg/m^3	- 0.001 / + 0.012	3.8×10^{-4} - 6.2×10^{-4}	-1.57×10^{-6}	2000 ±840	- 0.0033 ± 0.0014	674±250	~ 0.945	~ 0.994
$\gamma^n = 28.094$ kg/m^3	+ 0.001 / + 0.009	0.4×10^{-4} - 3.5×10^{-4}	-1.65×10^{-6}	2180 ±480	- 0.0036 ± 0.0008	418±470	~ 0.806	~ 0.696

634

635   To determine $d^{232}Th_p/dz$, we use the Niskin filtration data because they have a better vertical

636   resolution. We determine $d^{232}Th_p/dz$ based on the $^{232}Th_p$ concentrations measured above and

26

637   below the depth of the neutral density surface at each station (Fig. 9). For γ^n = 27.865 kg/m^3,

638   d^{232}Th$_p$/dz varies strongly between S1 and S4. Interestingly, we obtain low d^{232}Th$_p$/dz values

639   when the ^{232}Th$_t$ horizontal gradient is low (e.g., d^{232}Th$_p$/dz = - 0.001 pg/kg/m at S3) and

640   higher d^{232}Th$_p$/dz values when the ^{232}Th$_t$ horizontal gradient is high (e.g., d^{232}Th$_p$/dz = +

641   0.006 pg/kg/m at S1). In other words, the increase of ^{232}Th$_t$ with depth is due to the horizontal

642   transport of ^{232}Th by eddy diffusion from the margin, whereas without inputs from the

643   margins the dissolved and particulate ^{232}Th concentration would be expected to be constant

644   with depth (Roy-Barman et al., 1996). Ideally, it would be best to integrate equation 7 with

645   d^{232}Th$_p$/dz and d^{230}Th$_p$/dz varying with x. In practice, it is difficult to determine the evolution

646   of these gradients along the isopycnal or even to determine the exact average gradients

647   between stations S1 and S4. As a first approach, we will just use the range of the gradients

648   measured between S1 and S4 as input values to determine w$_p$, u$_i$ and K$_i$. For ^{232}Th, we use a

649   range d^{232}Th$_p$/dz from - 0.001 to + 0.012 pg/kg/m (Fig. 9, Tab. 1). For ^{230}Th, most ^{230}Th$_p$ data

650   plot along a slope ranging between 3.8×10^{-4} fg/kg/m and 6.2 ×10^{-4} fg/kg/m (Fig. 9, Tab. 1).

651   We then estimate w$_p$ and u$_i$ with a least square approach. Using Monte Carlo

652   simulations, we maximize the coefficient of determination (R^2) of the ^{230}Th$_t$ versus S and

653   ^{232}Th$_t$ versus S curves simultaneously. In equation 9, w$_p$ and the dTh$_p$/dz terms are present as

654   products so that their opposite variations cancel each other. As a consequence, a relatively

655   large range of w$_p$, d^{230}Th$_p$/dz and d^{232}Th$_p$/dz values yield similar R^2 values. Therefore, we

656   report w$_p$ and u$_i$ obtained for a range of high R^2 values. We obtain w$_p$ = 674 ± 250 m/y and u$_i$

657   = - 0.0033 ± 0.0014 m/s. Using the u$_i$/K$_i$ ratio estimated previously, we deduce K$_i$ = 2000 ±

658   840 m/s^2.

659

660   <u>γ^n = 28.094</u> kg/m^3

661   For γ^n = 28.094 kg/m^3, most of the ^{230}Th$_p$ data plot along a slope of 5×10^{-4} fg/kg/m,

662   whereas ^{232}Th$_p$ data plot along a slope of 2×10^{-4} pg/kg/m (Fig. 10). In both diagrams, the

663   slope of the S4 station is poorly defined and potentially lower than the average. Using the

664   same method, we obtain u$_i$/K$_i$ = - 1.65×10^{-6} m^{-1}, w$_p$ = 435 ± 324 m/y, u$_i$ = - 0.0036 ± 0.0008

665   m/s and K$_i$ = 2180 ± 480 m/s^2 (Fig 8-9, Tab. 1).

666

667   The 2 K$_i$ values estimated here are on the upper end of the range (300 to 1800 m^2/s) reported

668   in the Southern Ocean, whereas u$_i$ is on the lower but of the same order of magnitude than an

669   estimate of the cross-stream horizontal velocity associated with the upwelling in the ACC (~ -

670   0.010 ± 0.003 m/s, Naveira Garabato et al., 2007, Zika et al., 2009).

671

672   We have estimated w_p at relatively close depths on the 2 isopycnals (1200-1500 m for $\gamma^n =$

673   27.865 kg/m^3 at stations S3 and S2 and 1000-1200 m for $\gamma^n = 28.094$ kg/m^3 at stations intercal

674   and S4, Fig. ES2). Taking the corresponding w_p at face value (but keeping in mind that they

675   strongly rely on the particulate concentration gradient estimate), it seems that there is a

676   southward decrease of w_p (for $\gamma^n = 27.865$, $w_p = 600$ m/y and for $\gamma^n = 28.094$ kg/m^3, $w_p = 300$

677   m/y). This southward decrease of settling speed seems consistent with the ^{238}U-^{234}Th

678   disequilibrium in the surface waters that decreased from the north to the south of the polar

679   front zone (PFZ) during the BGH cruise (Planchon et al., 2013) and 2 weeks earlier on the

680   same transect during the ANTXXIV/3 cruise (Rutgers van der Loeff et al., 2011). This

681   gradient of the ^{238}U-^{234}Th disequilibrium indicates a higher removal rate of ^{234}Th and suggests

682   a higher particle settling velocity in the north compared the south of the PFZ.

683

684   It is rewarding that the particle settling speeds obtained with the isopycnal mixing model

685   (which does not integrate the conservation equation over the water column) are in the range of

686   the speeds generally obtained with the vertical 1D model (see section 4.1; Rutgers van der

687   Loeff and Berger, 1993). In the 1D production-scavenging model, w_p is given by (see section

688   4.1.): $w_p = P/(d^{230}Th_p/dz)$. However, w_p is usually obtained by averaging $(d^{230}Th_p/dz)$ over

689   the whole water column or a large part of the water column as we did in section 4.1.

690   Consequently, the w_p does not depend on sharp changes of $(d^{230}Th_p/dz)$ that could result from

691   random errors on $^{230}Th_p$ at intermediate depths. In the 1D mixing-scavenging model some

692   advection is introduced but the model is still integrated from the surface to the seafloor, so

693   that random errors on $^{230}Th_p$ tend to be smoothed out (Rutgers van der Loeff and Berger,

694   1993). In addition, ^{234}U *in situ* decay is not the only source of dissolved ^{230}Th, because

695   advection also brings dissolved and particulate ^{230}Th, which adds up uncertainty on the input

696   rate of ^{230}Th.

697   In the isopycnal mixing model presented here, the uncertainties cited above can have much

698   larger effects on w_p because i) $(d^{230}Th_p/dz)$ is calculated over much thinner depth ranges and

699   ii) combined effects of high water flow rates and small ^{230}Th concentration gradients implies

700   that the net effect of circulation on ^{230}Th transport is subject to large relative uncertainties.

701   Nevertheless, the isopycnal mixing model opens the possibility to calculate the vertical

702   evolution of w_p in highly dynamical environments where the hypotheses of the 1D model are

703   clearly not fulfilled.

704

705   In a recent series of paper, non-linear dissolved ^{230}Th profiles are modelled with a

706   purely 1D approach by adjusting adsorption/desorption/remineralization rates and particle

707   settling velocities that are assumed to vary with depth (Lerner et al., 2016, 2017 and 2018).

708   These numerous parameters are adjusted by using different Th isotopes (^{228}Th, ^{230}Th, ^{234}Th).

709   This approach is different but not inconsistent with our approach because: (1) Unlike the

710   present paper, Lerner et al focus on areas where advection and eddy diffusion are expected to

711   be negligible; (2) In the present paper, we make no hypothesis on the processes driving

712   dissolved-particulate transfers (Eq. 7). Ultimately, it should be possible to determine

713   adsorption/desorption rates in areas with weak currents and then to use these values in regions

714   with a vigorous circulation such as the ACC. Lerner's approach treats explicitly the case of w_p

715   varying with depth, whereas our approach to leave the possibility to determine the particle

716   settling speed at different depths/density. To do so rigorously, it will be necessary to treat w_p

717   like a parameter varying with depth (see section 4.3).

718

719   5. Conclusion

720   While we still used crude approximations, the model proposed here opens the

721   possibility to determine the particle settling speed and to bring constraints on the isopycnal

722   mixing rate at different vertical levels and with a more realistic description of the vertical

723   structure of the water column. The improvement that will come out of the method proposed

724   here will require sampling with higher horizontal and vertical sampling resolutions, a goal

725   partly achieved in the framework of the GEOTRACES program. It also requires progresses

726   for the particulate Th analysis and constant efforts for the intercalibration of the different

727   cruises.

728

729

730

731

732

745 **References :**
746 Abadie, C., Lacan, F., Radic, A., Pradoux, C., Poitrasson, F., 2017. Iron isotopes reveal
747   distinct dissolved iron sources and pathways in the intermediate versus deep Southern
748   Ocean. Proceedings of the National Academy of Sciences, 114(5), 858-863.
749 Anderson, R.F., Fleisher, M.Q., Robinson, L.F., Edwards, R.L., Hoff, J. a., Moran, S.B.,
750   Loeff, M.R. Van Der, Thomas, A.L., Roy-Barman, M., Francois, R., 2012. GEOTRACES
751   intercalibration of ^{230}Th, ^{232}Th, ^{231}Pa, and prospects for ^{10}Be. Limnol. Oceanogr. Methods
752   10, 179–213.
753 Arhan, M., Mercier, H., Park, Y.-H., 2003. On the Deep Water circulation of the eastern
754   South Atlantic Ocean. Deep-Sea Research Part I 50, 889–916.
755 Bacon, M.P., Anderson, R.F., 1982. Distribution of Thorium isotopes between dissolved and
756   particulate forms in the deep sea. J. Geophys. Res. 87, 2045–2056.
757   doi:10.1029/JC087iC03p02045
758 Bown, J., Boye, M., Baker, A., Duvieilbourg, E., Lacan, F., Le Moigne, F., ... Nelson, D. M.,
759   2011. The biogeochemical cycle of dissolved cobalt in the Atlantic and the Southern Ocean
760   south off the coast of South Africa. Marine Chemistry 126, 193-206.
761 Chever, F., Bucciarelli, E., Sarthou, G., Speich, S., Arhan, M., Penven, P., Tagliabue, A.,
762   2010. Physical speciation of iron in the Atlantic sector of the Southern Ocean along a
763   transect from the subtropical domain to the Weddell Sea Gyre. Journal of Geophysical
764   Research: Oceans, 115(C10).
765 Chase, Z., Anderson, R. F., Fleisher, M. Q., Kubik, P. W., 2003. Scavenging of ^{230}Th, ^{231}Pa
766   and ^{10}Be in the Southern Ocean (SW Pacific sector): The importance of particle flux,
767   particle composition and advection. Deep Sea Research Part II: Topical Studies in
768   Oceanography 50, 739-768.
769 Coppola, L., Roy-Barman, M., Mulsow, S., Povinec, P., Jeandel, C., 2006. Thorium isotopes
770   as tracers of particles dynamics in the Indian sector of the Southern Ocean. Marine
771   Chemistry 100, 299-313
772 Dutay, J.-C., Lacan, F., Roy Barman, M. and Bopp, L., 2009. The influence of particle size
773   and type on ^{231}Pa and ^{230}Th simulation with a global coupled biogeochemical- ocean
774   general circulation model: a first approach. G-cubed, doi:10.1029/2008GC002291
775 Garcia-Solsona, E., Jeandel, C., Labatut, M., Lacan, F., Vance, D., Chavagnac, V., Pradoux,
776   C., 2014. Rare earth elements and Nd isotopes tracing water mass mixing and particle-
777   seawater interactions in the SE Atlantic. Geochimica et Cosmochimica Acta, 125, 351-372.
778 Gdaniec, S., Roy-Barman, M., Foliot, L., Thil, F., Dapoigny, A., Burckel, P, A. Masque, P.,
779   Garcia-Orellana, J., Morth, M., Andersson, P. S., 2018. Thorium and protactinium isotopes
780   as tracers of marine particle fluxes and deep water circulation in the Mediterranean Sea.
781   Marine Chemistry 199, 12-23.
782 Gdaniec, S., Roy-Barman, M., Levier, M., Valk O., Rutgers van der Loeff, M., Foliot, L.,
783   Dapoigny, A., Morth, M., Andersson, P. S., 2019. ^{231}Pa and ^{230}Th in the Arctic Ocean:
784   implications for Boundary Scavenging and ^{231}Pa-^{230}Th fractionation in the Eurasian Basin.
785   Submitted to Chemical Geology
786 Gladyshev S., Arhan M., Sokov A., Speich S., 2008. A hydrographic section from South
787   Africa to the southern limit of the Antarctic Circumpolar Current at the Greenwich
788   meridian. Deep-Sea Res. I 55, 1284–1303.

789   Gu, S., Liu, Z., 2017. ^{231}Pa and ^{230}Th in the ocean model of the Community Earth System
790   Model (CESM1.3), Geosci. Model Dev., 10, 4723-4742

791   Jeandel, C., Venchiarutti, C., Bourquin, M., Pradoux, C., Lacan, F., van Beek, P., Riotte, J.,
792   2011. Single column sequential extraction of Ra, Nd, Th, Pa and U from a natural sample.
793   Geostand. Geoanalytical Res. 35, 449–459.

794   Jenkins, W. J., 1987. ^{3}H and ^{3}He in the Beta Triangle: Observations of gyre ventilation and
795   oxygen utilization rates. J. Phys. Oceanogr. 17, 763-783.

796   Lerner, P., Marchal, O., Lam, P. J., Anderson, R. F., Buesseler, K., Charette, M. A., Edwards,
797   R. L., Hayes, C. T., Huang, K. F., Lu, Y., Robinson, L. F., Solow, A., 2016. Testing
798   models of thorium and particle cycling in the ocean using data from station GT11-22 of the
799   US GEOTRACES North Atlantic Section, Deep Sea Research Part I: Oceanographic
800   Research Papers, 113, 57–79.

801   Lerner, P., Marchal, O., Lam, P. J., Buesseler, K., Charette, M., 2017. Kinetics of thorium and
802   particle cycling along the US GEOTRACES North Atlantic Transect. Deep Sea Research
803   Part I: Oceanographic Research Papers, 125, 106-128.

804   Lerner, P., Marchal, O., Lam, P. J., Solow, A., 2018. Effects of particle composition on
805   thorium scavenging in the North Atlantic. Geochimica et Cosmochimica Acta, 233, 115-
806   134.

807   Marshall, J., Speer, K., 2012. Closure of the meridional overturning circulation through
808   Southern Ocean upwelling. Nature Geoscience 5, 171-180.

809   Naveira Garabato, A.C., Stevens, D.P., Watson, A.J. and Roether, W., 2007. Short-circuiting
810   of the overturning circulation in the Antarctic Circumpolar Current. Nature 447|, 194-197.

811   Nozaki, Y., Horibe, Y., Tsubota, H., 1981. The water column distribution of thorium isotopes
812   in the western North Pacific, Earth Planet. Sc. Lett., 54, 203–216.

813   Planchon, F., Cavagna, A. J., Cardinal, D., André, L., Dehairs, F., 2013. Late summer
814   particulate organic carbon export and twilight zone remineralisation in the Atlantic sector
815   of the Southern Ocean. Biogeosciences 10, 803-820.

816   Planquette, H., Sherrell, R. M., 2012. Sampling for particulate trace element determination
817   using water sampling bottles: methodology and comparison to in situ pumps. Limnology
818   and Oceanography: methods 10, 367-388.

819   Roy-Barman, M., 2009. Modelling the effect of boundary scavenging on Thorium and
820   Protactinium profiles in the ocean. Biogeosciences 6, 7853–7896.

821   Roy-Barman, M., Chen, J.H., Wasserburg, G.J., 1996. The sources and the fates of thorium.
822   Earth Planet. Sci. Lett. 139, 351–363.

823   Roy-Barman, M., Coppola, L., Souhaut, M., 2002. Thorium isotopes in the western
824   Mediterranean Sea: An insight into the marine particle dynamics. Earth Planet. Sci. Lett.
825   196, 161–174.

826   Rutgers van der Loeff, M.M., Berger, G.W., 1993. Scavenging of ^{230}Th and ^{231}Pa near the
827   antarctic polar front in the South Atlantic. Deep. Res. Part I 40, 339–357

828   Rutgers van der Loeff, R., Cai, P. H., Stimac, I., Bracher, A., Middag, R., Klunder, M. B., &
829   van Heuven, S. M., 2011. ^{234}Th in surface waters: distribution of particle export flux across
830   the Antarctic Circumpolar Current and in the Weddell Sea during the GEOTRACES
831   expedition ZERO and DRAKE. Deep Sea Research Part II: Topical Studies in
832   Oceanography 58, 2749-2766.

833 Rutgers van der Loeff, M., Venchiarutti, C., Stimac, I., van Ooijen, J., Huhn, O., Rohardt, G.,
834   & Strass, V., 2016. Meridional circulation across the Antarctic Circumpolar Current serves
835   as a double ^{231}Pa and ^{230}Th trap. Earth and Planetary Science Letters, 455, 73-84.

836 Schlitzer, R., 2007. Ocean data view. http://odv. awi. de.

837 Scholten, J. C., Fietzke, J., Mangini, A., Garbe-Schönberg, C. D., Eisenhauer, A., Schneider,
838   R., Stoffers, P., 2008. Advection and scavenging: Effects on 230Th and 231Pa distribution
839   off Southwest Africa. Earth and Planetary Science Letters, 271(1), 159-169.

840 Sims, K. W., Gill, J. B., Dosseto, A., Hoffmann, D. L., Lundstrom, C. C., Williams, R. W., ...
841   Glessner, J. J., 2008. An inter-laboratory assessment of the thorium isotopic composition
842   of synthetic and rock reference materials. Geostandards and Geoanalytical Research 32,
843   65-91.

844 Sokolov, S., Rintoul, S. R., 2009. Circumpolar structure and distribution of the Antarctic
845   Circumpolar fronts: 1. Mean circumpolar path, J. Geophys. Res., 114, C11018,
846   doi:10.1029/2008JC005108.

847 Thomas, A.L., Henderson, G.M., Robinson, L.F., 2006. Interpretation of the 231A/230Th
848   paleocirculation proxy: new water-column measurements from the southwest Indian
849   Ocean. Earth Planet. Sci. Lett. 241, 493.

850 van Hulten, M. M. P., Dutay, J. C., Roy-Barman, 2018. A global scavenging and circulation
851   ocean model of thorium-230 and protactinium-231 with an improved particle dynamics
852   (NEMO–ProThorP 0.1). Goescientific model development 11, 3537-3556.

853 Venchiarutti, C., Jeandel C., Roy-Barman, M., 2008. Particle dynamics in the wake of
854   Kerguelen Island traced by thorium isotopes (Southern Ocean, KEOPS program). Deep
855   Sea Research I 55, 1343-1363

856 Venchiarutti, C., van der Loeff, M.R., Stimac, I., 2011. Scavenging of ^{231}Pa and thorium
857   isotopes based on dissolved and size-fractionated particulate distributions at Drake Passage
858   (ANTXXIV-3). Deep. Res. Part II Top. Stud. Oceanogr. 58, 2767–2784.

859 Walter, H.J., Rutgers van der Loeff, M.M., Hoeltzen, H., 1997. Enhanced scavenging of ^{231}Pa
860   relative to ^{230}Th in the South Atlantic south of the Polar Front: Implications for the use of
861   the ^{231}Pa/^{230}Th ratio as a paleoproductivity proxy. Earth Planet. Sci. Lett. 149, 85–100.

862 Watson A. J., Ledwell J. R., Messias M. J., King B. A., Mackay N., Meredith M. P., Mills B.,
863   and Garabato A. C. N., 2013. Rapid cross-density ocean mixing at mid depths in Drake
864   Passage measured by tracer release. Nature 501, 408–413.

865 Zika, J. D., Sloyan, B. M. & McDougall, T. J., 2009. Diagnosing the Southern Ocean
866   overturning from tracer fields. J. Phys. Oceanogr. 39, 2926-2940.

867
868
869
870
871
872
873
874
875
876

Table ES1: Dissolved Thorium data.

Station	Depth (m)	θ (°C)	Salinity	γ^n (kg/m³)	$^{232}Th_d$[1] (pg/kg)	$^{230}Th_p$[1] (pg/kg)	$^{230}Th_{p\text{-}xs}$[2] (pg/kg)	Water mass
S1: 36.50°S, 13.10°E, 4923 m bottom depth								
	29	20.785	35.617	25.0222	34.7 ± 1.3	1.21 ± 0.03	1.06 ± 0.03	ICW
	198	12.364	35.014	26.53	52.1 ± 1.3	2.48 ± 0.04	2.25 ± 0.04	ICW
	397	9.824	34.757	26.7918	50.1 ± 1.5	4.52 ± 0.06	4.30 ± 0.06	ICW
	753	4.973	34.346	27.1602	37.2 ± 1.3	5.45 ± 0.08	5.29 ± 0.08	i-AAIW
	1188	3.279	34.551	27.5004	38.0 ± 1.3	7.38 ± 0.12	7.22 ± 0.12	i-AAIW
	1975	2.515	34.808	27.7752	40.2 ± 1.4	11.64 ± 0.18	11.46 ± 0.18	SE-NADW
	2664	2.132	34.838	27.8316	42.0 ± 1.3	14.71 ± 0.19	14.52 ±0.19	SE-NADW
	3005	1.945	34.836	27.8444	42.2 ± 1.4	14.94 ± 0.17	14.76 ± 0.17	SE-NADW
	3981	0.892	34.749	27.8506	70.0 ± 1.4	17.55 ± 0.23	17.25 ± 0.23	AABW
	4565	0.716	34.733	27.8493	69.1 ± 1.6	21.70 ± 0.27	21.40 ±0.27	AABW
	4907	0.568	34.72	27.8481	288.5 ± 3.5	37.10 ± 0.41	35.84 ± 0.41	AABW
S2: 42.47°S, 08.93°E, 4070 m bottom depth								
	20	12.951	34.521	26.0547	11.1 ± 1.4	0.74 ± 0.02	0.70 ± 0.03	ICW
	124	9.083	34.482	26.7815	19.8 ± 1.4	1.84 ± 0.03	1.75 ± 0.04	ICW
	292	6.654	34.267	27.0053	36.2 ± 1.3	3.04 ± 0.04	2.89 ± 0.04	ICW/a-AAIW
	398	6.01	34.292	27.1231	38.8 ± 1.5	4.13 ± 0.06	3.97 ± 0.06	ICW/a-AAIW
	595	4.138	34.185	27.2829	30.9 ± 1.4	5.14 ± 0.08	5.01 ± 0.08	a-AAIW
	940	3.075	34.313	27.5162	25.7 ± 1.3	7.02 ± 0.09	6.90 ± 0.09	a-AAIW
	1453	2.626	34.585	27.7945	26.1 ± 1.3	9.19 ± 0.11	9.07 ± 0.11	UCDW
	2172	2.346	34.79	27.994	31.1 ± 1.3	13.36 ± 0.16	13.22 ± 0.16	SE-NADW
	2905	1.967	34.827	28.0789	35.8 ± 1.3	14.43 ± 0.16	14.28 ± 0.16	SE-NADW
	3445	1.427	34.792	28.1359	36.9 ± 1.6	16.13 ± 0.24	15.96 ± 0.24	SE-NADW
	4021	0.81	34.741	28.1961	63.9 ± 1.5	17.96 ± 0.22	17.68 ± 0.22	AABW
S3: 47.55°S, 04.37°E, 4480 m bottom depth								
	40	6.32	33.733	26.5685	7.5 ± 1.4	1.19 ± 0.04	1.15 ± 0.04	AASW
	124	4.029	33.867	27.0072	8.3 ± 1.3	1.82 ± 0.04	1.79 ± 0.04	AASW
	248	3.633	34.101	27.2697	15.3 ± 1.4	3.55 ± 0.07	3.48 ± 0.07	AASW/a-AAIW
	495	2.739	34.233	27.4888	17.1 ± 1.2	5.07 ± 0.07	5.00 ± 0.07	a-AAIW
	742	2.591	34.407	27.6574	16.8 ± 1.3	6.46 ± 0.11	6.39 ± 0.11	a-AAIW/UCDW
	1068	2.447	34.575	27.8099	18.2 ± 1.3	8.26 ± 0.10	8.18 ± 0.10	A_UCDW
	1482	2.334	34.716	27.936	22.2 ± 1.5	10.93 ± 0.17	10.83 ± 0.17	SW-NADW
	2003	1.971	34.771	28.0376	23.2 ± 1.2	12.68 ± 0.15	12.58 ± 0.15	SW-NADW
	2003				23.2 ± 1.5	13.45 ± 0.16	13.34 ± 0.16	
	3052	0.955	34.731	28.1653	29.2 ± 1.6	14.94 ± 0.19	14.81 ± 0.19	SW-NADW
	4299	0.415	34.695	28.2262	18.5 ± 1.3	8.83 ± 0.12	8.75 ± 0.12	AABW

S4: 51.85°S, 00.00°E, 2570 m bottom depth								
59	2.521	33.712	27.0277	4.7 ± 1.5	1.20 ± 0.03	1.18 ± 0.03	AASW
168	0.827	34.033	27.4838	10.8 ± 1.5	2.82 ± 0.06	2.77 ± 0.06	WW (AASW)
248	1.543	34.433	27.7832	13.4 ± 1.6	5.04 ± 0.08	4.98 ± 0.08	WW/DP-UCDW
327	1.811	34.548	27.8553	13.8 ± 1.6	6.64 ± 0.10	6.58 ± 0.10	DP-UCDW
416	1.874	34.627	27.9165	17.4 ± 1.3	8.68 ± 0.10	8.61 ± 0.10	DP-UCDW
416	1.874	34.627	27.9165	15.7 ± 1.3	7.94 ± 0.10	7.87 ± 0.10	DP-UCDW
742	1.702	34.704	28.012	21.5 ± 1.5	12.16 ± 0.14	12.06 ± 0.14	LCDW
1117	1.42	34.727	28.08	27.3 ± 1.3	15.28 ± 0.17	15.16 ± 0.17	LCDW
1678	0.755	34.704	28.171	28.6 ± 1.5	16.70 ± 0.19	16.58 ± 0.19	LCDW/AABW
2307	0.359	34.689	28.225	30.5 ± 1.4	18.11 ± 0.21	17.98 ± 0.21	AABW
2501	0.319	34.687	28.231	30.1 ± 1.3	16.82 ± 0.19	16.69 ± 0.19	AABW
Intercal: 52.98°S, 00.00°W, 2624 m bottom depth								
380	1.81	34.63	27.929	19.1 ± 1.2	9.93 ± 0.13	9.85 ± 0.13	UCDW
380	1.81	34.63	27.929	19.6 ± 1.4	9.90 ± 0.12	9.82 ± 0.12	UCDW
500	1.78	34.68	27.979	22.0 ± 1.2	12.14 ± 0.14	12.05 ± 0.14	LCDW
500	1.78	34.68	27.979	24.5 ± 1.5	13.44 ± 0.20	13.33 ± 0.20	LCDW
1000	1.22	34.71	28.094	27.4 ± 1.2	16.08 ± 0.20	15.96 ± 0.20	LCDW
1000	1.22	34.71	28.094	27.5 ± 1.3	16.11 ± 0.18	15.99 ± 0.18	LCDW
S5: 57.55°S, 00.03°W, 3932 m bottom depth								
134	-0.671	34.355	27.8713	19.7 ± 1.5	8.26 ± 0.11	8.17 ± 0.11	WW (AASW)
247	0.353	34.63	28.094	29.4 ± 1.5	15.64 ± 0.19	15.51 ± 0.19	WW (AASW)/ WDW
396	0.529	34.674	28.154	32.8 ± 1.4	19.10 ± 0.24	18.96 ± 0.24	WDW
692	0.422	34.685	28.202	36.1 ± 1.5	23.00 ± 0.24	22.84 ± 0.24	WDW
1185	0.154	34.677	28.2434	42.2 ± 1.5	26.59 ± 0.29	26.41 ± 0.29	WDW / WSDW
1776	-0.104	34.668	28.2872	49.4 ± 1.6	30.31 ± 0.32	30.10 ± 0.32	WDW / WSDW
2462	-0.346	34.66	28.332	60.6 ± 1.4	34.30 ± 0.36	34.04 ± 0.36	WSDW
3147	-0.502	34.655	28.3619	71.5 ± 1.6	34.42 ± 0.36	34.10 ± 0.36	WSDW
3848	-0.632	34.65	27.8713	83.1 ± 1.6	33.93 ± 0.37	33.57 ± 0.37	WSDW / WSBW
3848	-0.632	34.65	27.8713	82.5 ± 1.8	33.78 ± 0.38	33.42 ± 0.38	WSDW / WSBW

887   [1]: Uncertainties are $2\sigma_n$ (error on the mean). [2]: The excess $^{230}Th_{d-xs}$ is calculated using the

888   equation:

889    $^{230}Th_{d-xs} = \ ^{230}Th_{d-measured} - \ ^{232}Th_{d-measured} \times \left(\frac{^{230}Th}{^{232}Th}\right)_{Lithogenic}$, where the

890    $(^{230}Th/^{232}Th)_{Litogenic} = 4.0 \times 10^{-6}$ (mol/mol), close to average crust $^{230}Th/^{232}Th = 4.1 \times 10^{-6}$).

891   The lithogenic correction is small: generally less than 2% of $^{230}Th_d$ and occasionally reaching

892   6 to 11% in the surface waters of S2 and S1 respectively. Therefore the $^{230}Th_d$ and $^{230}Th_{d-xs}$

893   profiles do not differ significantly.

894

895

896

897

Table ES2: Particulate thorium data (in situ pump filtration)

Station	Depth (m)	Volume[1] (L)	$^{232}Th_p$ (pg/kg)[2]	$^{230}Th_p$ (pg/kg)[2]	$^{230}Th_{p-xs}$ (pg/kg)[2]	$^{230}Th_{p-xs}$ particulate fraction
S1						
	30	346	7.0 ± 0.1	0.076 ± 0.002	0.045 ± 0.003	4 %
	199	803	18.8 ± 0.3	0.209 ± 0.004	0.128 ± 0.004	6 %
	1242	997	32.3 ± 0.7	1.45 ± 0.03	1.31 ± 0.03	18 %
	2687	142	37.8 ± 0.5	1.309 ± 0.003	1.144 ± 0.004	8 %
	2732	1202	17.3 ± 0.5	1.8 ± 0.4	1.7 ± 0.4	12 %
	4628	610	371 ± 10	28.1 ± 0.4	26.5 ± 0.4	124 %
S2						
	20	315	4.1 ± 0.1	0.148 ± 0.004	0.130 ± 0.004	18 %
	257	814	8.9 ± 0.1	0.379 ± 0.003	0.340 ± 0.003	12 %
	601	961	5.4 ± 0.1	0.492 ± 0.004	0.469 ± 0.004	9 %
	1426	1053	9.1 ± 0.1	1.462 ± 0.009	1.422 ± 0.009	16 %
	1941	531	8.5 ± 0.1	0.752 ± 0.005	0.715 ± 0.005	5 %
	2859	515	8.9 ± 0.1	1.63 ± 0.01	1.59 ± 0.01	11 %
	3858	508	93.1 ± 1.2	8.51 ± 0.07	8.10 ± 0.07	48 %
S3						
	40	99	7.1 ± 0.1	0.163 ± 0.002	0.133 ± 0.002	12 %
	594	500	4.41 ± 0.04	0.686 ± 0.002	0.667 ± 0.002	13 %
	1058	967	5.1 ± 0.1	1.045 ± 0.003	1.023 ± 0.003	12 %
	1985	1128	5.5 ± 0.1	1.426 ± 0.004	1.402 ± 0.004	13 %
	3025	218	7.7 ± 0.1	1.778 ± 0.006	1.745 ± 0.006	12 %
	3024	552	8.0 ± 0.1	1.838 ± 0.005	1.804 ± 0.005	12 %
	4262	210	2.5 ± 0.0	0.344 ± 0.002	0.333 ± 0.002	4 %
S4						
	59	381	0.076 ± 0.001	0.0202 ± 0.0005	0.0198 ± 0.005	2 %
	169	702	1.48 ± 0.02	0.300 ± 0.001	0.294 ± 0.001	11 %
	258	903	2.42 ± 0.02	0.467 ± 0.001	0.457 ± 0.001	9 %
	743	984	2.23 ± 0.02	0.682 ± 0.002	0.672 ± 0.002	6 %
	1119	1069	2.82 ± 0.03	0.630 ± 0.002	0.617 ± 0.002	4 %
	1120	308	1.72 ± 0.02	0.368 ± 0.002	0.360 ± 0.002	2 %
	1682	1018	2.23 ± 0.02	0.727 ± 0.002	0.717 ± 0.002	4 %
	2273	938	6.07 ± 0.06	1.885 ± 0.005	1.858 ± 0.005	10 %
	2469	493	6.25 ± 0.06	1.850 ± 0.005	1.823 ± 0.005	11 %
S5						
	30	341	2.23 ± 0.01	0.706 ± 0.005	0.697 ± 0.005	
	139	872	2.1 ± 0.1	0.261 ± 0.002	0.251 ± 0.002	3 %
	248	927	2.5 ± 0.1	0.507 ± 0.003	0.496 ± 0.003	3 %
	694	127	3.6 ± 0.8	0.555 ± 0.009	0.539 ± 0.010	2 %
	1784	290	4.0 ± 0.4	0.714 ± 0.006	0.697 ± 0.006	2 %
	2478	1066	8.5 ± 0.1	1.726 ± 0.029	1.69 ± 0.03	5 %
	3172	905	11.6 ± 0.2	1.754 ± 0.006	1.703 ± 0.006	5 %
	3840	715	26.1 ± 0.3	2.966 ± 0.012	2.852 ± 0.012	8 %

899 [1] Fraction of the volume of filtered water used for Thorium analysis. [2] Uncertainties are $2\sigma_n$
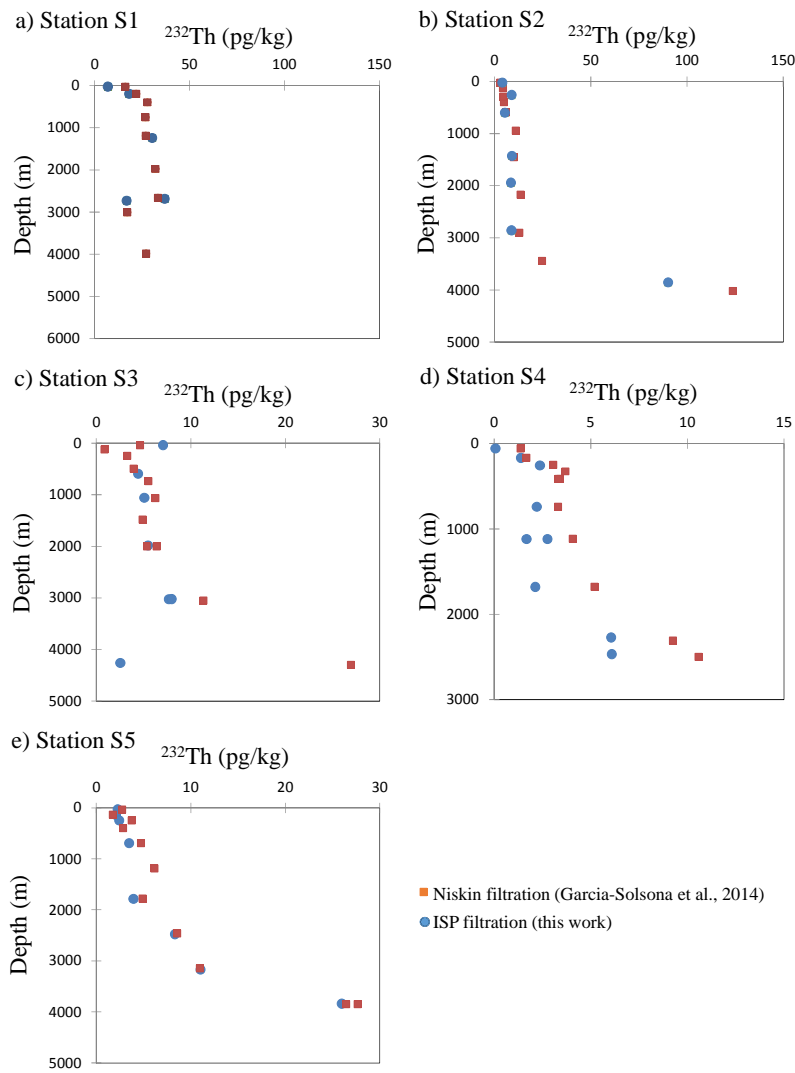900 (error on the mean).
901

902

903

904 Table ES3: Total thorium isotopes recalculated on neutral density surfaces

	Depth (m)	θ (°C)	Salinity	^{232}Th (pg/kg)	error	^{230}Th (fg/kg)	error
γ^n = 27.865 kg/m^3							
S1	-1550	2.732	34.695	10.67	0.15	72.4	1.5
S2	-1631	2.564	34.667	11.51	0.12	36.3	1.3
S3	-1227	2.44	34.644	10.07	0.13	25.1	2.9
S4	-345	1.838	34.563	7.59	0.11	16.8	1.8
S5	-98	-0.665	34.348	8.52	0.11	21.8	0.1
γ^n = 28.094 kg/m^3							
S1	3073	1.86	34.827	15.1	0.2	60.7	1.5
S2	3082	1.849	34.823	17.3	0.8	52.9	0.2
S3	2440	1.722	34.756	15.2	0.2	32.1	1.3
S4	1205	1.322	34.726	15.9	0.2	29.3	1.3
intercal	-999.6	1.205	34.71	16.7	0.2	30.1	1.2
intercal	-999.6	1.205	34.71	16.7	0.2	30.2	1.3
S5	247	0.28616	34.619	16.1	0.2	31.9	1.6

905

906   Fig. ES1: comparison of particulate [232]Th collected by in situ pump and Niskin filtrations.

a) Station S1

b) Station S2

c) Station S3

d) Station S4

e) Station S5

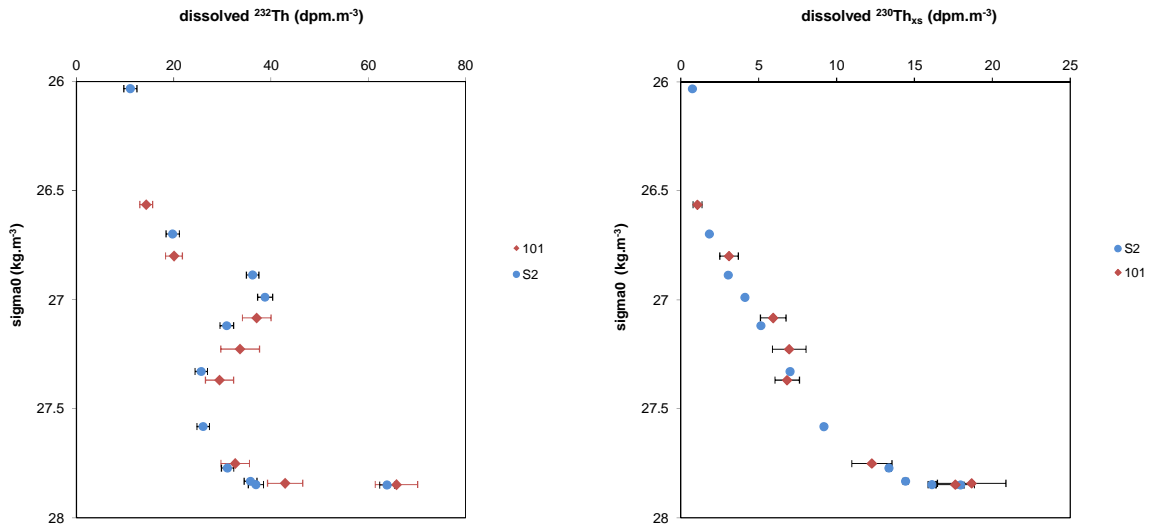■ Niskin filtration (Garcia-Solsona et al., 2014)
● ISP filtration (this work)

907

908

Figure ES2: Dissolved Th isotopes BGH sections. (a) ^{232}Th$_d$. (b): ^{230}Th$_d$. White curves:
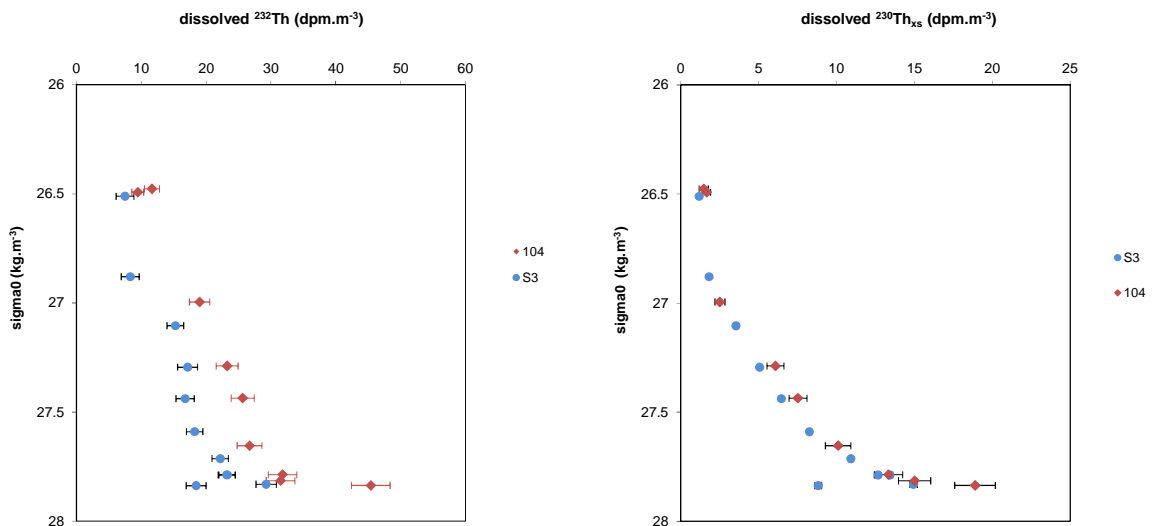910 neutral density surfaces.
911
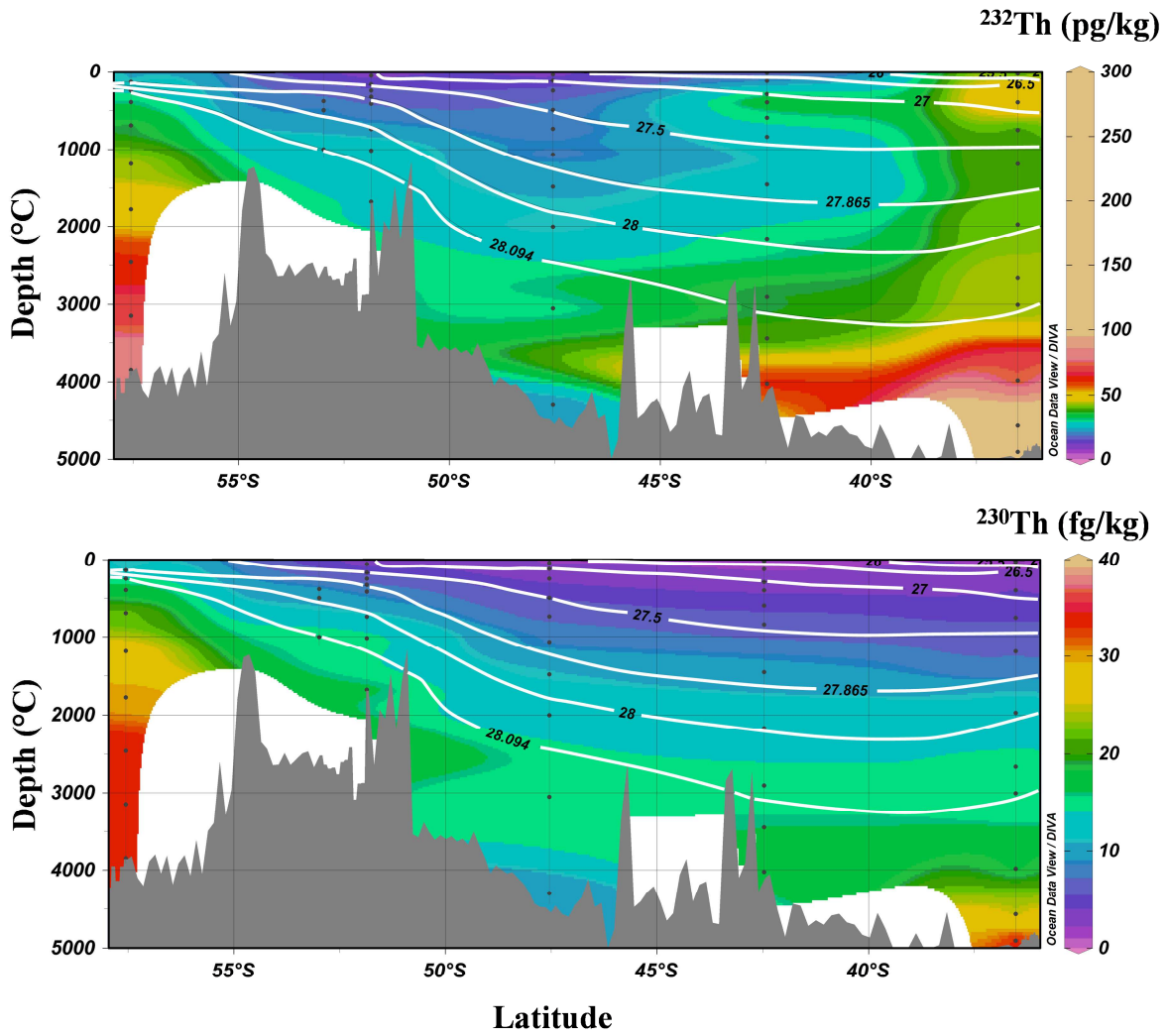
912
913
914
915
916
917
918

919

920

921　Figure ES3: Dissolved Th comparison between 2 stations of the BGH and Zero-Drake
922　sections. $^{232}Th_d$ and $^{230}Th_d$ are plotted versus potential density anomaly in order to reduce
923　hydrographical variations between the 2 cruises.

924

925

926

927

928

929

930

931

932